Highlights

- Pleistocene pedogenic carbonates in eastern Sudan are mainly calcretes and nodules.
- An initially semi-arid climate that became more humid and then semi-arid again.
- A mixture of C_3 and C_4 vegetation cover was present.
- Mean annual precipitation was likely greater than 350 mm/yr and similar to today.
- Calcretes formed in floodplains in a climate similar to that in East Africa.

Pleistocene pedogenic carbonates from alluvial paleosols in eastern Sudan reveal a semi-arid and seasonal climate, similar to today

Mosab Mohammednoor[a, b*], Faysal Bibi[b], Ulrich Struck[b], Ali Eisawi[c], Robert Bussert[a]

[a]Technische Universität Berlin, Institute of Applied Geosciences, Ernst-Reuter-Platz 1, 10587 Berlin, Germany.

[b]Museum für Naturkunde, Leibniz Institute for Evolution and Biodiversity Science, Invalidenstrasse 43, 10115 Berlin, Germany.

[c]Al Neelain University, Faculty of Petroleum and Minerals, El Gamhuriya Avenue, 11121 Khartoum, Sudan.

*Corresponding Author: mosab.ma.mohammednoor@campus.tu-berlin.de

This manuscript has been published in Catena Journal with DOI: https://doi.org/10.1016/j.catena.2024.108583

Abstract

Pedogenic carbonates can provide important information regarding paleoclimatic conditions. Compared with East Africa, Pleistocene pedogenic carbonates in Sudan, particularly calcretes, have received very little attention, particularly with regard to local paleoclimatic reconstructions. Pleistocene alluvial sediments aged from ~230 to <17 ka were deposited along the middle Atbara River in eastern Sudan. Intercalated in these alluvial deposits are paleosols in which different types of pedogenic carbonates occur. Petrographic, mineralogical and isotopic analyses were performed to reconstruct the regional paleoenvironmental conditions. The investigated pedogenic carbonates are appropriate for paleoclimatic reconstruction because they are free of inherited carbonate and diagenetic modification. The paleosols identified in a previous study as Aridisols/Calcisols contain calcrete horizons that consist of an orthic nodular horizon, sometimes overlain by a laminar horizon. Paleosols identified as Vertisols contain slickensides, and disorthic and septaric nodules. The paleosols show stable carbon and oxygen isotope values ranging between -9.12 and -5.12 ‰, and between -7.25 and -4.09 ‰, respectively. Supporting the previous study, the inferred climatic conditions were arid to semi-arid, with a mixture of C_3 and C_4 vegetation cover, and paleoprecipitation greater than 350 mm/yr, similar to that of the present-day, with likely higher rainfall during the formation of Vertisols than Aridisols/Calcisols. The thickness and morphology of Pleistocene calcretes in eastern Sudan are similar to those in East Africa, suggesting similar climatic conditions during their formation. Well-and weakly-developed calcretes in Aridisols formed in distal and proximal floodplains, respectively, whereas well-developed vertic horizon in Vertisols formed in distal floodplains.

Keywords: Pleistocene, pedogenic carbonates, Sudan, East Africa, paleoclimate.

1. Introduction

Pedogenic carbonates develop in soils as rhizoliths, nodules, and calcretes, from geogenic carbonate parent materials, biogenic carbonates and previously formed pedogenic carbonates (Zamanian et al., 2016; Durand et al., 2018). Rhizoliths are organosedimentary structures resulting in the preservation of roots in mineral matter (Klappa, 1980). They formed by mass flow of water with soluble Ca^{2+} towards the root and precipitation of calcium carbonate along the root (Zamanian et al., 2016). Nodules are formed by the impregnation of the soil matrix with calcium carbonate at specific locations (Durand et al., 2018). They occur in a wide variety of forms, nodules with diffuse or irregular boundaries are orthic, those with sharp boundaries are disorthic, and anorthic nodules are characterized by different fabrics from the groundmass (Wieder and Yaalon, 1974; Stoops, 2021). Calcretes are surface-near accumulations of calcium carbonate, where vadose and shallow phreatic groundwater become saturated in calcium carbonate (Wright, 2007). Calcrete formation occurs in soil profiles, bedrock, and sediments in various forms, ranging from powdery to indurated (Wright and Tucker, 1991; Wright, 2007). Netterberg (1969, 1980), Esteban and Klappa (1983) and Goudie (1983) provided a morphological classification for calcretes based on their development in the soil profile. The early stage of calcrete formation begins with a calcareous soil or a chalky horizon (Goudie, 1983), which, over time, passes to a nodular horizon, to a hardpan, and later to boulder or pisolithic calcrete. These maturity-related stages are similar to those of the Gile et al. (1966) and Machette (1985) models, in which six stages -ranging from I to VI- of calcrete development were identified based primarily on the texture of the parent material and carbonate accumulation. Pedogenic carbonates form in a variety of climates, particularly in semi-arid to arid areas, where the carbonate sources in the soil profile are dissolved. The dissolved Ca^{2+} ions are translocated by water movement in various directions, whether downward (leaching) or upward (capillary rise), and when the supersaturation of the soil solution with $CaCO_3$ takes place due to evapotranspiration and decreasing pCO_2 in the soil air, pedogenic carbonate is precipitated (Zamanian et al., 2016). Pedogenic carbonates are important proxies of paleoenvironmental changes (Durand et al., 2018). Mesozoic and Cenozoic calcretes form important archives for paleoclimatic and paleoenvironmental reconstruction (Horn et al., 2013; Kaplan et al., 2013; Khalaf and Al-Zamel, 2016; Srivastava et al., 2019; Valera-Fernández et al., 2020; Jarraya et al., 2024). Neogene to Holocene calcretes in East Africa were morphologically described and used to reconstruct paleoclimatic conditions during their formation and typically indicate semi-arid conditions (Cerling et al., 1977; Hay and Reeder, 1978; Cerling and Hay, 1986; Levin et al., 2011; Owen et al., 2014; Felske, 2016).

In Sudan, pedogenic carbonates, particularly calcretes have received less attention than those in East Africa. Dawelbeit et al. (2019) suggested that the nodular and tabular (root) calcretes in Late Pleistocene-Holocene aeolian and palustrine limestone deposits in the Kordofan region of western Sudan formed in an arid and humid climate, respectively. Sasso et al. (2018) pointed out that a calcrete horizon in Aridisols on the western bank of the White Nile in central Sudan consists of nodular and powdery calcretes of Early and Middle Holocene age. The former indicates short arid phases during generally wetter climate conditions and the latter indicates more humid phases than the climatic conditions in which the nodular calcrete was formed. Modern Vertisols, Entisols, Aridisols, and Alfisols in Central Sudan are characterized by pedogenic carbonates in the form of spots, powder and nodules, particularly Aridisols contain calcic and petrocalcic horizons (Blokhuis et al., 1969; Buursink, 1971; Blokhuis, 1993). Investigation of Pleistocene calcretes in Sudan in terms of their stage of development and paleoclimate significance and comparing them with their counterparts in East Africa can provide a better understanding of the environmental history of the region during this period. Pleistocene alluvial sediments, dated from ~230 to <17 ka, are exposed with a maximum thickness of 50 m along the middle stretches of the Atbara River in eastern Sudan (Abbate et al., 2010; Tsukamoto et al., 2022), which is the last major tributary of the Nile before it flows to the Mediterranean. Intercalated in these alluvial sediments are paleosols, characterized by either pedogenic carbonates or pedogenic carbonates and slickensides. The paleosols were previously identified as Aridisols/Calcicsols and Vertisols indicating an arid to semi-arid and a seasonal humid climate, respectively (Mohammednoor et al., 2024). The given age ranges of Aridisols/Calcisols are 212 ± 18-187 ± 15 ka, 166 ± 11-164 ± 11 ka, 161 ± 11-160 ± 11 ka, 148 ± 11-145 ± 11 ka and 22 ± 3 to ~14 ka, and Vertisols are 123 ± 10-114 ± 10 ka, 98 ± 10-90 ± 10 ka and 64 ± 9-40 ± 7 ka (Mohammednoor et al., 2024).

Here, we studied pedogenic carbonates, particularly calcretes in the Pleistocene alluvial sediments of the middle Atbara River by using petrographic, mineralogical, and isotopic analyses. This investigation aimed to reconstruct the paleoclimate and paleolandscape of the study area. It supports and supplements the results of Mohammednoor et al. (2024) regarding the Pleistocene paleoclimate in the study area.

2. Environmental Setting

The study area is located along the Atbara River near the Butana Bridge, north of Khashm El Girba (Fig. 1). The study area lies on the northern rim of the Cretaceous Gedaref Basin (Eisawi and Schrank, 2009), which is surrounded by Precambrian rocks (Fig. 1). During the Cenozoic, basaltic lava flows, dikes, and sills formed in the Gedaref Basin, in connection with the uplift of the Ethiopian highlands and widespread flood basalt volcanism (Vail, 1988). Since the Middle Pleistocene, precursor rivers of the modern Atbara River have incised into the Cretaceous sediments and the Cenozoic volcanics. The alluvial deposits of these rivers contain several erosional unconformities, which indicate multiple periods of river incision. Based on these unconformities, Abbate et al. (2010) divided the sedimentary sequence into two major sedimentary units: the older Butana Bridge Synthem (BBS) and the younger Khashm El Girba Synthem (KGS), which were subdivided into three intervals (BBS1-3) or subsynthems (KGS1-3). Each subsynthem comprises sandy to gravelly channel deposits at the base, overlain by fine-grained floodplain deposits containing paleosols and low-thickness channel deposits (Fig. 2). Due to the incision of the present-day Atbara River into the sediments after the deposition of the KGS3 unit, the entire sedimentary sequence from the BBS to the KGS3, with a thickness of approximately 40 m, is now exposed along the middle course of the river around Khashm El Girba.

Luminescence dating revealed ages of ~220–160 ka, ~160–130 ka, ~130–30 ka and ~30– < 17 ka for the BBS1-3, KGS1, KGS2 and KGS3, respectively (Tsukamoto et al., 2022; Fig. 2), reflecting that the deposition was continuous with no major gaps between the sedimentary units.

Today, the region's climate is semi-arid, with a mean annual temperature of 28°C and mean annual rainfall ranging from ~400 to ~600 mm (Buursink, 1971; Blokhuis, 1993; Mirghani, 2002). The vegetation cover is a woodland savanna mainly characterized by trees and bushes of *Acacia mellifera* (Harrison and Jackson, 1958; Abdelmalik et al., 2024). Modern Vertisols, Entisols, Aridisols and Alfisols are present, with wide occurrence of Vertisols (Buursink, 1971; Blokhuis, 1993; Williams, 2019).

3. Materials and Methods

3.1. Field methods

Pedogenic carbonates from the Pleistocene paleosols, intercalated with alluvial sediments (Fig. 2) along the Atbara River, were investigated in the surroundings of the Butana Bridge near the village of Al Sharafa. Paleosols were examined in the field, and those characterized by the most representative pedogenic features were selected for investigation and sampling (Fig. 2). Paleosol profiles were measured and described (Fig. 3). Sampling locations for the BBS2, BBS3, KGS1 and KGS3 Aridisols/Calcisols were, respectively: 15° 04' 39.3" N, 35° 57' 29.2" E; 15° 04' 38.6" N, 35° 57' 29.5" E; 15° 04' 26.1" N, 35° 57' 31.5" E; 15° 04' 28.7" N, 35° 56' 29.1" E, and for the KGS2 Vertisol: 15° 04' 57.3" N, 35° 56' 56.4" E. 14 samples of pedogenic carbonate were collected from investigated paleosol profiles for carbonate content determination and bulk mineralogical, micromorphological, and isotopic analyses (Table 1; Fig. 3). The color of the paleosols was determined using the Munsell Capsure Color Matching Tool RM200SOIL, and calcareous rhizoliths were classified as root casts and root petrifications following Klappa (1980). In February 2022, a sample of local groundwater from the Butana Bridge area and four samples of Atbara River from the Butana Bridge area and further south in the Khashm El Girba and Wadi Turk areas were collected for isotopic analysis (Table 1). Eight blocks of undisturbed oriented paleosol samples were extracted from BBS2 and KGS (1-3) paleosols for micromorphological analysis (Table 1; Fig. 3).

Nodular calcretes were identified as consisting of discrete nodules embedded in a less carbonate-rich matrix, and laminar calcretes as consisting of indurated sheets with abundant rhizoliths, usually, but not always, overlain by indurated rock (Netterberg, 1980; Esteban and Klappa, 1983; Goudie, 1983). To describe the stages of calcrete development, the classifications proposed by Gile et al. (1966) and Machette (1985) were used.

The classification of boundaries between calcrete horizons, size and abundance of calcareous nodules and size of blocky peds follows the Soil Survey Staff (2017).

3.2. Laboratory methods

3.2.1. Carbonate content

The carbonate content of the pedogenic carbonates was determined following the "Karbonat-Bombe" method based on Müller and Gastner (1971). For the carbonate content of the matrix in the calcrete horizons, see Mohammednoor et al. (2024).

3.2.2. X-ray diffraction (XRD)

XRD was used in identifying the bulk mineralogy of pedogenic carbonates; the bulk mineralogy of the paleosols was previously analyzed by Mohammednoor et al. (2024). Samples were pulverized using a McCrown mill, mounted on a silicon crystal holder, and measured with a Burker D2 diffractometer using Cu- Kα radiation and operated with 30 kV and 10 mA. Diffraction data was recorded from 3° to 80° 2θ with a step width of 0.02° and a time of 0.5 s per step. The DIFFRAC.SUITE EVA (Bruker) software, equipped with the PDF-4 mineral database, was used to identify the minerals from the positions of the diffracted peaks. The peak position of the quartz (101) at 26.644° 2θ was used to correct the peak positions. The magnesium content of calcite in the pedogenic carbonates was determined by measuring the position of the d_{104} peak of calcite in the diffractogram, which displaces depending on the $MgCO_3$ content in the calcite lattice (Goldsmith et al., 1961).

3.2.3. Optical microscopy

Pedogenic carbonate and oriented paleosol samples were sawed into blocks and immersed in Araldite 2020 epoxy resin. After removing excess resin and to obtain a flat surface, samples were ground smooth on one side using grinding plates, and then manually lapped. The samples were then glued onto a 1500 µm thick glass slide and sawed using Conrad WOCO rock saw, ground to a thickness of ~1700 µm (sample and glass) with a MPS grinder, lapped with a Logitech machine to a thickness of ~1525 µm and finally polished. The thin sections were examined micromorphologically using a Zeiss Axioplan polarizing microscope equipped with a Leica Flexacam C3 digital camera. To identify pedogenic features, we followed the guidelines of Wright and Tucker (1991), Durand et al. (2018), Kovda and Mermut (2018) and Verrecchia and Trombino (2021).

3.2.4. Pedogenic carbonate carbon ($\delta^{13}C$) and oxygen ($\delta^{18}O$) isotopic analysis

The isotopic composition of pedogenic carbonate can be used as a paleoclimatic and paleoecological indicator (Cerling, 1984). The $\delta^{13}C$ value of soil carbonate is controlled by the relative abundance of C_3, primarily trees and shrubs, and C_4, mainly grasses and sedges, plants in the local vegetation that grew in the soil during the period of pedogenic carbonate formation (Cerling and Quade, 1993). The $\delta^{18}O$ value of pedogenic carbonate is related to the $\delta^{18}O$ value of the meteoric water from which it is derived and the temperature of carbonate mineral crystallization (O'Neil et al., 1969; Cerling, 1984). Isotope measurements were conducted on pulverized pedogenic carbonate and water samples at the Museum für Naturkunde, Leibniz Institute for Evolution and Biodiversity Science.

For oxygen and carbon isotope measurements of pedogenic carbonate samples, approximately 100-400 micrograms of sample material were put into a clean 10 ml exetainer. After sealing the exetainer with a septum cap (caps and septa for LABCO exetainer 438b) the remaining air was removed by flushing the exetainer with helium (4.6) for 6 minutes at a flow of 100 ml/minute. After flushing, approximately 30 microliters of anhydrous phosphoric acid were injected through the septum into the sealed exetainer by using a disposable syringe and left for approximately 1.5 hours of reaction time at 50°C.

The oxygen and carbon isotopic composition in the CO_2 in the headspace were measured using a Thermo Fisher Scientific GASBENCH II coupled online with a Thermo Fisher Scientific DELTA V isotope ratio mass spectrometer. Reference gas was pure CO_2 (4.5) from a cylinder calibrated against the Vienna PeeDee Belemnite (VPDB) using International Atomic Energy Agency (IAEA) reference materials (NBS 18, NBS 19). Isotope values are shown in the conventional delta-notation (^{18}O, ^{13}C) in per mil (‰) relative to the VPDB. The reproducibility of replicate measurements of lab standards (limestone) is generally better than 0.10‰ (one standard deviation).

Stable isotope ratios of oxygen ($^{18}O/^{16}O$) in water samples were measured with a PICARRO L1102-i isotope analyzer. The L1102-i is based on the wavelength-scanned cavity ring down spectroscopy technique (WS-CRDS; Gupta et al., 2009). Measurements were calibrated by the application of linear regression of the analyses of IAEA calibration material Vienna Standard Mean Ocean Water (VSMOW), Vienna Standard Light Antarctic Precipitation and Greenland Ice Sheet Precipitation. The stable isotope ratio of oxygen is expressed in the conventional delta-notation (^{18}O) in permil (‰) versus VSMOW. For each sample, 6 replicate injections were performed, and the arithmetic average and standard deviations (1 sigma) were calculated. The reproducibility of replicate measurements is generally better than 0.1 ‰ for oxygen.

The proportion of C_4 biomass in the study area was calculated based on $\delta^{13}C$ values of the studied pedogenic carbonates and the average $\delta^{13}C$ values of C_3 and C_4 plants, which are -27 ‰ and -12 ‰, respectively (Cerling et al., 1997), using the following linear mixing equation (Eq. 1; Fox and Koch, 2003):

$$X*C_4+(1-X)*C_3= \delta^{13}C_{CaCO3}-15.5‰ \qquad (1)$$

where X is the C_4 %.

The fraction of woody cover (f_{wc}) was estimated based on $\delta^{13}C$ values of the studied pedogenic carbonates using the following equation (Eq. 2; Cerling et al., 2011):

$$f_{wc}\ [\sin(-1.06688-0.08538(\delta^{13}C_{CaCO3}-14))]^2 \qquad (2)$$

4. Results

4.1. Field description

The BBS and KGS paleosols in the outcrops were identified in the alluvial sediments that contain them by coloration, presence of pedogenic carbonates (calcareous nodules, root casts and calcretes), slickensides and soil peds (Fig. 2). The base of BBS2 contains two paleosol profiles in which horizons of calcretes are present. The basal and upper parts of the BBS3 interval are also distinguished by calcretes-bearing paleosol profiles. The middle part of unit KGS1 contains two paleosol profiles marked by calcretes and blocky peds. The multiple paleosols intercalated in unit KGS2 exhibit well-developed vertic features and calcareous nodules. A calcrete-bearing paleosol is present in the upper part of unit KGS3. The paleosols are organic-matter-poor and comprise only B horizons.

The examined paleosol in the BBS2 interval (Fig. 3e) is mainly calcretes consisting of laminar and nodular horizons from top to bottom. The profile is a 110 cm thick, medium beige (10 Yellow-Red (YR) 8/6), and horizontally bedded. The upper horizon is a 10 cm thick indurated, slightly laminar, and calcareous roots mat characterized by 0.3-1 cm long root casts. An abrupt (0.5-2 cm wide) boundary is present between this horizon and the underlying nodular horizon, possibly pointing to an erosional surface (Retallack, 2019). Approximately 1 cm of laminar calcrete fills the desiccation cracks in the underlying nodular horizon. The nodular horizon is a 100 cm thick and comprises scattered calcareous nodules that are coarse to very coarse (0.5-7 cm diameter), irregular in shape, and common (2-20 % of the exposed surface). It contains a non-calcareous to slightly calcareous matrix and abundant calcareous root casts with lengths of up to ~15 cm and diameters of up to ~10 cm.

The paleosol investigated in the BBS3 interval (Fig. 3d) shows a 100 cm thick horizon of nodular calcretes. The profile is horizontally bedded, light beige (10 YR 5/3) at the bottom, and medium beige in the upper part. The nodules are irregular, medium to coarse (0.2-2 cm diameter), and few (< 2 % of the exposed surface) to common. The matrix is a non-calcareous to calcareous, and calcareous root casts with a length of 1-5 cm and a thickness of 0.2-0.5 cm are abundant.

The paleosol in KGS1 (Fig. 3c) varies in color from medium beige at the bottom, dark beige (10 YR 6/4) in the middle and light beige at the top. It contains a 70 cm thick horizon of nodular calcretes marked by abundant and scattered calcareous root casts 1-5 cm long and 0.2-0.5 cm thick and very fine (size < 0.5 cm) angular blocky peds. The nodules are few to common, irregular, and fine to medium (> 0.2-0.5 cm), and the matrix in the horizon is a non-calcareous to slightly calcareous.

The studied paleosol profile in the KGS2 is a 140 cm thick (Fig. 3b), non-calcareous to slightly calcareous, massive and medium beige. It characterized by vertic features such as well-developed slickensides, fine (0.5-1 cm) to medium (1-2 cm) size angular blocky peds, and Fe /Mn oxide nodules at the bottom. It contains pedogenic carbonates such as nodules and root casts. The nodules are few, irregular, and medium to coarse, whereas the root casts are also few, scattered with a length of ~0.5-3 cm and a thickness of 0.2-0.5 cm.

A 160 cm thick, highly calcareous light beige laminar and nodular calcretes horizon (Fig. 3a) forms the upper part of KGS3. The upper laminar horizon is a 20 cm thick, indurated, and slightly laminar, but mostly a massive calcareous roots mat characterized by root casts with a length of 0.3-1 cm. An abrupt boundary separates the upper horizon (laminar) and the underlying nodular horizon, which is a 140 cm thick and distinguished by a calcareous matrix, and many (> 20 % of the exposed surface) scattered, irregular, and medium to coarse nodules.

4.2. Mineralogy

The laminar horizons in the BBS2 and KGS3 calcretes have carbonate contents of ~55 % and ~48% in the root casts (see Supplementary Data 1), and the matrix contains ~40% and ~33% carbonates, respectively. The nodular horizons in the BBS2 and KGS3 calcretes contain nodules with carbonate contents of ~45% and ~48%, which embedded in a matrix with carbonate contents of up to ~13% and ~18%, respectively. Nodules in the nodular horizons in the BBS3 and KGS1calcretes consist of ~38 % and ~33 % carbonates (see Supplementary Data 1), and the carbonate content in the matrix reaches ~15 %, and ~7 %, respectively. Nodules in the KGS2 Vertisol contain approximately 57% carbonate and are embedded in a matrix with a carbonate content of up to 8%. Based on field observations and the carbonate content in the matrix, the laminar horizons in the BBS2 and KGS3 calcretes correspond to calcrete stages IV and V, and the nodular horizons in the BBS2, BBS3, KGS1 and KGS3 calcretes to stage II calcrete according to the calcrete development stages proposed by Gile et al. (1966) and Machette (1985).

In addition to carbonates (calcite and dolomite), the paleosols and pedogenic carbonates contain quartz, feldspar, hornblende, halite, mordenite, mica/illite, and clay minerals such as chlorite and smectite (Fig. 4). Additionally, the paleosol samples include trace amounts of gypsum in the upper part of the KGS3 paleosol. The content of $MgCO_3$ in calcite in the analyzed pedogenic carbonates ranges between 0.11 and 2.81 mole % (see Supplementary Data 1), indicating the presence of only low-Mg calcite, whence Netterberg (1980) and Hardy and Tucker (1988) suggested that the threshold of low- to high Mg calcite is 4 and 5 mole % of $MgCO_3$, respectively.

4.3. Micromorphology

4.3.1. Pedogenic carbonates

The pedogenic carbonates show an open porphyric pattern, in which quartz, calcite, feldspar, and biotite grains are scattered in a dense micritic matrix (Fig. 5a), which is denser in the nodular horizons than in the roots mat horizons. Crack voids (Fig. 5b) dominate in KGS2, whereas in BBS, KGS1 and KGS3 channel voids, interconnected channel (chamber) voids and vug voids are prominent.

Pedofeatures such as carbonate coatings and infillings (Fig. 5b, c) characterize most of the pedogenic carbonates, in which desiccation cracks are coated or filled by only one generation of sharply contacted sparitic calcite (Fig. 5b). Additionally, some floating quartz and feldspar grains in the micritic matrix are partially surrounded by pores (Fig. 5d, e), indicating the dissolution of silicate minerals under high pH conditions in arid conditions (Durand et al., 2018). These pedofeatures and the absence of biological activity-related features indicate that most of the calcretes in the study area are of Alfa fabric (Wright, 1990a). The roots mat horizon in BBS2 exhibits Beta fabric, characterized by calcium carbonate petrified roots (Fig. 5f), in which the cellular structure of the decayed roots is filled with sparitic calcite. Spherical to ellipsoidal and micritic pellets (Fig. 5g) are also present.

4.3.2. Paleosols

The paleosols also display an open porphyric pattern. Quartz, calcite, feldspar, muscovite, biotite, amphibole and basalt fragments are scattered in a dense siltic matrix (Fig. 6a, b) in the BBS, KGS1 and KGS3 paleosols, and a dense clayic matrix is present in the KGS2 paleosol.

The BBS and KGS3 paleosols mainly show calcium carbonate-related pedofeatures, such as sparitic and micritic void coatings that are thicker in KGS3 (Fig. 6c), sparitic to micritic, mostly mammillate (undulating external shape; Stoops, 2003), typic (structureless internal fabric; Bullock et al., 1985), and orthic (diffuse or irregular boundary; Stoops et al., 2018; Fig. 6d) nodules. Additionally, micrite infillings (Fig. 6e) occupy some voids in the KGS3 paleosol.

The KGS1 paleosol also exhibits carbonate pedofeatures, such as void coatings and root cross-sections (Fig. 6f) filled with sparitic calcite with traces of Fe/Mn oxides. Additionally, it contains features indicative of leaching, such as clay illuviations (Verrecchia and Trombino, 2021), in which the clay coats voids, quartz, and feldspar grains (Fig. 6g, h).

Vertic features resulting from shrink-swell processes in clayey materials are widespread in the KGS2 paleosol. Argilliturbation (Schaetzl and Thompson, 2015; Fig. 6i) and a striated groundmass formed from clay translocation (Verrecchia and Trombino, 2021) mark the KGS2 paleosol. Angular blocky peds (aggregates; Fig. 6j) with a high to moderate degree of separation are present between the planar voids, which represent cracks. Clay coatings occur along these planar pores and exhibit a striated b-fabric that is parallel to each other (parallel striated b-fabric; Fig. 6k) in some parts of the groundmass, indicating pedogenic slickensides (Mermut et al., 1996; Kovda and Mermut, 2018). Additionally, clay illuviations occur around grains. Unlike in the BBS and KGS3 paleosols, the carbonate nodules are microsparitic to micritic, but the latter are more abundant because of the clayic soil matrix, typic and disorthic (sharp boundary; Stoops et al., 2018; Fig. 6l) or septaric (radiating cracks in the center; Bullock et al., 1985: Fig. 6m) micritic nodules. These nodule types often result from shrinkage and swelling (Stoops et al., 2018; Stoops and Marcelino, 2018).

4.4. $\delta^{13}C$ and $\delta^{18}O$ isotope values

The $\delta^{13}C$ and $\delta^{18}O$ values are relatively homogeneous across the studied pedogenic carbonates ranging between -9.12 and -5.12 ‰ with a mean of -7.09 ‰, and between -7.25 and -4.09 ‰ with a mean of -5.9 ‰, respectively (Fig. 7a; see Supplementary Data 2). Comparisons between the BBS and KGS2, the only units from which more than two samples of pedogenic carbonate were taken, show similar $\delta^{13}C$ values (Fig. 7a, b), but more depleted in $\delta^{18}O$ in the KGS2 (Fig. 7c). In the BBS2 and KGS3 calcretes, the roots mat horizons show lower $\delta^{13}C$ values than the underlying micritic nodular horizons.

The $\delta^{18}O$ values of the waters from which pedogenic carbonate precipitated can be calculated if the temperature is known (Kim and O'Neil, 1997). Using the relationship between the oxygen isotope values of carbonate and water (Zhou and Chafetz, 2010), and the present mean annual temperature in the study area (28ºC), the range of the $\delta^{18}O$ values of soil solutions in the Pleistocene is estimated to vary from -4.22 ‰ to -1 ‰ with an average of -2.83 ‰ (Fig. 8). This is less enriched than the present Atbara River (average = 2.47 ‰; see Supplementary Data 3) and local groundwater (0.22 ‰; see Supplementary Data 3) in the vicinity of Al Sharafa village. Our estimates of Pleistocene soil water $\delta^{18}O$ are however similar to rainy season water in summer of the modern Shinfa River, a tributary of the Blue Nile in northwestern Ethiopia (average =~ -2 ‰; Tabor et al., 2021), and to the precipitation in Sudan as measured in August and September 2021 (average = - 3.66 ‰; IAEA/World Meteorological Organization, https://www.iaea.org/services/networks/gnip).

5. Discussion

5.1. Assessing the viability of the pedogenic carbonates for paleoclimate reconstructions

Pedogenic carbonates can contain inherited carbonate or be mineralogically and chemically altered after formation (Zamanian et al., 2016), which may lead to false paleoclimate reconstruction. However, this is most likely not the case for the pedogenic carbonate samples investigated. Microscopic analysis shows that the pedogenic carbonates are free of inherited carbonate, such as allochthonous limestone fragments. Additionally, the orthic calcareous nodules in the BBS and KGS3 paleosols, which are similar in fabric to the surrounding groundmass, as well as the absence of anorthic nodules in the sedimentary units, indicate that the carbonate nodules formed in situ and are not allochthonous (Wieder and Yaalon, 1974; Stoops, 2021). The isotopic composition of the studied pedogenic carbonates does not show a large variation (Fig. 7a), which suggests that they are not modified by diagenetic overprinting (Richoz et al., 2017), such as recrystallization. The absence of significant diagenetic change is supported by microscopic evidence, as the pedogenic carbonates contain sparite (coarse calcite crystals) in the form of filling or coating of voids, whereas coarse calcite crystals are absent in the micritic (fine crystalline) matrix (Durand et al., 2018). Additionally, sharp contacts (Fig. 5b) with no pronounced serration between sparitic calcites are evidence of the absence of dissolution (Durand et al., 2018). Because the pedogenic carbonates in the study area seem free of inherited carbonate and diagenetic influence, they are suitable for paleoclimatic reconstruction.

5.2. Paleoclimatic implications

Pedogenic calcretes form because of the accumulation of calcium carbonate in the B horizon of soils due to intense evapotranspiration, predominantly in arid and semi-arid climates (Alonso-Zarza, 2003; Zamanian et al., 2016). The calcrete horizons in the BBS2, BBS3, and KGS1 paleosols indicate an arid to semi-arid climate during their formation. Generally, arid or semi-arid climatic conditions are also supported by the dominance of Alfa fabrics and the microscopic features of the pedogenic carbonates, such as coatings, infillings, and nodules in the BBS and KGS1 calcretes, which indicate high evaporation rates under arid to semi-arid conditions (Wright and Tucker, 1991; Durand et al., 2018). Additionally, the high carbonate content, such as seen in the roots mat horizon in the BBS2 calcrete, and the presence of evaporite minerals, such as halite in the BBS and KGS1 paleosols, suggest arid conditions during calcrete formation in these units.

Laminar calcretes occur either at the top of calcrete horizons, embedded in sedimentary deposits or at the top of any type of rock substrate, with the formation of root mats controlled by low water availability (Netterberg, 1980; Goudie, 1983; Wright et al., 1995; Alonso-Zarza, 1999, 2003; Alonso-Zarza and Silva, 2002; Zhou and Chafetz, 2009; Alonso-Zarza and Wright, 2010; Durand et al., 2018; Rodrigues et al., 2019). In the BBS2 calcrete, roots extend horizontally at the top of the profile; the roots obviously tried to obtain a maximum amount of water in an arid environment (Alonso-Zarza, 1999; Alonso-Zarza and Silva, 2002). The low Mg-calcite in the laminar horizon, the abundance of long calcareous root casts in the nodular horizon, and the presence of vertical laminar calcretes filling desiccation cracks in the nodular horizon likewise indicate that the groundwater table was deep. Laminar calcretes require a long time to develop, often 3 ka to over 1 Ma (Leeder, 1975; Hawley et al., 1976; Hay and Reeder, 1978; Wright, 1990b; Candy et al., 2004). The presence of laminar calcrete at the top of the calcrete horizon is also an indicator of a high maturity stage (Alonso-Zarza and Silva, 2002). Therefore, the arid period during the formation of the BBS2 calcrete thus was most likely longer and warmer than in the BBS3 and KGS1. In the KGS1 calcrete, the angular blocky peds imply shrink-swell processes related to the wetting and drying of argillic soil (Tabor et al., 2017; Beverly et al., 2018; Retallack, 2019). Clay illuviations point to the presence of an argic horizon and, thus, a wetter climate during the formation of the KGS1 than the BBS. The calcified root remains with traces of

Fe/Mn oxides in the KGS1 also indicate water saturation or fluctuations of the groundwater table during a humid period (Vepraskas et al., 2018; Verrecchia and Trombino, 2021).

In the KGS2 paleosol, vertic features (slickensides) indicate intense pedoturbation caused by the shrinking and swelling of expandable clay minerals during wetting and drying (Retallack, 2019). Argilliturbation, parallel striated b-fabric, angular blocky peds, and septaric and disorthic nodules suggest alternating wet and dry periods (Kovda and Mermut, 2018). Additionally, clay illuviation around mineral grains and rock fragments points to the translocation of clay by water during humid periods (Fedoroff et al., 2018). The lighter oxygen isotopic values also suggest lower evaporation and wetter conditions than those during the formation of the other paleosols. Such climatic conditions are consistent with the results of Mohammednoor et al. (2024), who showed that the amount of smectite in the KGS2 is higher than in the BBS2, BBS3, KGS1 and KGS3, indicating seasonally humid conditions.

Similar to the BBS and KGS1, the presence of a calcrete horizon, the Alfa fabric, microscopic features associated with pedogenic carbonate, the high carbonate content, and evaporite minerals such as halite and gypsum in the KGS3 paleosol indicate a return to arid conditions. The near absence of calcareous root casts in the nodular horizon suggests poor soil drainage, which led to water being confined mainly to the uppermost part of the profile, above the nodular horizon. In arid conditions, the confined water above the nodular horizon encouraged plant roots to maximize the amount of water they absorb. They, therefore, grow preferentially laterally and develop sub-horizontal networks (Alonso-Zarza and Silva, 2002), and then a laminar horizon formed above the nodular horizon. Similar to the BBS2 calcrete, the laminar horizon at the top of the KGS3 calcrete indicates that the climate was warmer than in the BBS3 and KGS1. The thicker carbonate coatings in the KGS3 calcrete than those in the BBS2 suggest that the KGS3 formed under more arid conditions than the BBS2.

Since Aridisols/Calcisols and Vertisols within each stratigraphic unit share similar pedogenic features, we suggest that they formed under similar climatic conditions. Hence, four arid intervals (212 ± 18-187 ± 15 ka, 166 ± 11-164 ± 11 ka, 161 ± 11-160 ± 11 ka and 148 ± 11-145 ± 11 ka) occurred in the study area during formation of BBS and KGS1 Aridisols/Calcisols (calcrete horizons) which correspond to Marine Isotope Stages (MIS) 7-6, three humid episodes (123 ± 10-114 ± 10 ka, 98 ± 10-90 ± 10 ka and 64 ± 9-40 ±7 ka) during formation of KGS2 Vertisols (vertic horizon) which correspond to MIS 5-3, and arid phase (22 ± 3 to ~14 ka) during the formation of KGS3 Aridisols/Calcisols (calcrete horizon) which corresponds to MIS 2 (Fig. 9).

$\delta^{13}C$ values of soil carbonates in pure C_3 habitats average around -12 ‰ and in pure C_4 habitats around +2 ‰ (Zamanian et al., 2016). Accordingly, the $\delta^{13}C$ values of the pedogenic carbonate in the study area show a mixture of C_3 and C_4 vegetation. Although the climatic conditions during the formation of the KGS2 paleosol seem to have been more humid than those of the other paleosols, $\delta^{13}C$ values from all units together indicate the presence of ~15 to 40 % C_4 plants, with no significant differences among units. These values indicate a woodland/bushland/thicket/shrubland vegetation (Cerling et al., 2011; Fig. 7a, b). The similarity in the isotope values is attributed to the presence of the roots mat horizon (laminar calcretes) in the BBS2 and KGS3 calcretes, in which the $\delta^{13}C$ values are generally more negative (Tandon and Andrews, 2001) during calcretization due to dense vegetation cover.

Pleistocene soil water $\delta^{18}O$ values were estimated to be similar to those of modern-day precipitation in Sudan and to the Shinfa River in Ethiopia today, suggesting that the climatic conditions in the study area during the Pleistocene might have been similar to those of the present. Today, atmospheric moisture over Sudan and Ethiopia is largely supplied by the Indian and Atlantic Oceans, which explains the similarity in $\delta^{18}O$ values across this region. Mean annual precipitation in the region around Khashm El Girba ranges from ~400 mm in the north to ~600 mm in the south (Climatological Normals 1941-1970, Sudan Meterological Department; Mirghani, 2002). Areas receiving less than 350 mm have rainfall $\delta^{18}O$ values greater than -2 ‰ (Talma and Netterberg, 1983). In contrast, the studied pedogenic carbonates do not show $\delta^{18}O$ values higher than -2 ‰, implying that the annual rainfall during their formation was higher than ~350 mm. The high $\delta^{18}O$ values in the modern Atbara River relative to those of modern Shinfa River water and rain water in Sudan might result from high evaporation, which likely has increased since dams were constructed in the upstream area (Fig. 1b). The relatively high $\delta^{18}O$ values in the Al Sharafa groundwater might have arisen from evaporation/evapotranspiration after rainwater, or during runoff from irrigation using Atbara River water.

During the Pleistocene, calcretes formed widely in East Africa under semi-arid or arid conditions with low and probably seasonal rainfall (Felske, 2016). The Ndutu (50-400 ka) and Naisiusiu (16-22 ka) beds in the eastern part of Olduvai Gorge in northern Tanzania comprise calcretes formed in an arid climate (Cerling et al., 1977; Hay and Reeder, 1978; Cerling and Hay, 1986). The calcrete horizon typically consists of ~0.4-5 cm thick laminar calcretes that overlie ~30-100 cm thick massive calcretes that correspond to mature stage IV pedogenic calcretes and are derived from carbonatite ash, which was a dominant source for the calcium carbonate (Hay and Reeder, 1978). Three distinct pedogenic calcrete layers (350-50 ka) occur in the southern Kenya Rift Valley (Felske, 2016). The calcretes mark dry periods when wetlands or shallow lakes dried up and were exposed subaerially (Owen et al., 2014; Felske, 2016). The older calcretes are well-developed pisoidal calcretes, whereas the calcretes forming the present land surface are laminar to massive. At Lake Magadi in the southern Kenya Rift Valley, an extensive 300-200 ka old and up to 50 cm thick calcrete lies at the contact between the Oloronga Beds (780-300 ka) and the overlying High Magadi Beds (~23 ka 9 ka; Felske, 2016).

Our results indicate that the calcretes in the study area, particularly the BBS2 and KGS3 calcretes, have similar characteristics in terms of thickness and maturity as Late Pleistocene calcretes in East Africa, in which the calcrete horizons are capped by laminar or pisoidal calcretes (stage V, IV and VI calcretes). These characteristics suggest that the climatic conditions in the study area – mostly semi-arid and seasonal – were similar to those in East Africa during the Late Pleistocene.

5.3. Regional and global scale paleoclimatic comparison

During the arid periods when the BBS and KGS1 calcretes formed (212 ± 18-187 ± 15 ka, 166 ± 11-164 ± 11 ka, 161 ± 11-160 ± 11 ka and 148 ± 11-145 ± 11 ka), two distinctly humid intervals occurred in the Chew Bahir Lake region of Ethiopia, from ~275 to 210 ka and ~210 to 125 ka (Foerster et al., 2022). High lake levels also existed in the Lake Natron-Lake Magadi area in the southern Gregory Rift Valley at 240 and ~135 ka (Hillaire-Marcel et al., 1986). The aridity during the formation of the BBS and KGS1 calcretes appears to partially coincide with the Penultimate Glacial Period (PGP) in the late Middle Pleistocene (Cohen and Gibbard, 2019), but this is inconsistent with the extremely arid conditions (megadroughts) in tropical Africa between 135 and 70 ka (Cohen et al., 2007; Scholz et al., 2007; Fig. 9), when the water volume of lakes in East Africa was much reduced. The water level of Lake Malawi in southeast Africa was approximately 100 m lower than today between 133 and125 ka and 109 and 97 ka (Stone et al., 2011), and Lake Challa (equatorial East Africa) experienced severe drought between ~114 and ~97 ka (Moernaut et al., 2010). During these megadroughts, humid conditions prevailed in the study area from 123 ± 10 to 114 ± 10 ka and 98 ± 10 to 90 ± 10 ka.

The first and second humid intervals during the formation of the KGS2 paleosols (123 ± 10 to 114 ± 10 ka and 98 ± 10 to 90 ± 10 ka) may coincide with wet climatic conditions documented in the Goda Mea Cave in Ethiopia at ~129 and ~108 ka (Asrat et al., 2018), the first of the three humid episodes (125-93, 82-73 and 42-34 ka; Lamb et al., 2018) in Lake Tana, and the existence of a megalake in the White Nile River region in Sudan around 109 ka (Barrows et al., 2014). The three wet phases represented in the KGS2 paleosols may also correspond to the formation of S5, S4, and S2 sapropels in the Mediterranean Sea (124, 102, and 55 ka; Williams et al., 2015; Fig. 9). The third humid period documented in the KGS2 paleosols (64 ± 9-40 ±7 ka) may correspond to the humid climate recorded in Lake Challa from ~97 to ~20 ka (Moernaut et al., 2010). Around 70 ka, Lake Tanganyika, Lake Malawi (East Africa; Schloz et al., 2007), and Lake Bosumtwi (West Africa; Scholz et al., 2007; Gosling et al., 2022) experienced a rise in water level due to increasingly wetter conditions.

The aridity during the formation of the KGS3 calcrete (22 ± 3 to ~14 ka) correlates with arid climatic conditions during the Last Glacial Maximum (LGM), which are also documented in other paleoclimate archives from the region that show low lake levels during this period. For example, Chew Bahir Lake experienced a dry episode between ~30 and 10 ka (Foerster et al., 2022), and the desiccation of the White Nile headwaters and Sudd swamps in South Sudan occurred between ~27-18 ka (Williams, 2019; Leplongeon, 2021). In Lake Malawi, the lake level fell by about 100 m between 23 and 19 ka (Stone et al., 2011), and another dry period occurred between ~18- ~15 (Barker et al., 2007). The sediments of Lake Besaka in the Afar region of Ethiopia indicate a cold and dry climate between 20 ka and 15 ka (Abell and Williams, 1989), and Lake Tana and Lake Tanganyika were also affected by desiccation and drought between 16 ka and 15 ka (Felton et al., 2007; Lamb et al., 2007). The eastern part of the Gulf of Guinea in West Africa also experienced a cold and dry climate prior ~15 ka (Crosta et al., 2012; Kallweit et al., 2012; Marret et al., 2013).

Our results show that the climatic conditions in the study area from ~ 70 ka, especially during the LGM, are consistent with the global and regional climatic records (Fig. 9). Although the humid intervals during KGS2 do not correspond to the episodes of lake level rise in Lake Tana and Chew Bahir, they correspond to the main phases of extreme flooding of the White and Blue Nile, such as the Megalake White Nile, and the Mediterranean Sea sapropels. This variability in local climate in the region may be due to different contributions from atmospheric moisture sources such as the Indian Ocean, Atlantic Ocean, Mediterranean

Sea, and the Red Sea, which may play a role in the migration of the Intertropical Convergence Zone and Congo Air Boundary (Levin et al., 2011; Costa et al., 2014).

5.4. Paleolandscape

Based on the sedimentological characteristics of the deposits, the landscape during the deposition of BBS and KGS is interpreted as a low-gradient alluvial plain traversed by river channels bordered by extensive floodplains. This landscape probably resembled the present-day region of the lower Atbara River. Soil formation in alluvial environments and the properties of calcretes vary greatly depending on the distance to the river channel, positional stability of the rivers, and deposition and drainage conditions on the floodplain. Well-developed and poorly drained soils preferentially form on distal, fine-grained floodplains of river systems with stable channels and low sedimentation rates (Kraus, 1999; Alonso-Zarza, 2003). During the deposition of BBS and KGS, poorly fixed and repeatedly shifting braided rivers and more stabilized meandering rivers developed (Abbate et al., 2010; Mohammednoor et al., 2024). Paleosols formed predominantly in flood plains of relatively stable channels and reduced discharge (Mohammednoor et al., 2024).

In the BBS3 and KGS1 paleosols, the stage II calcretes indicate only weak calcrete development, and the calcareous root casts in the nodular horizon reveal a well-drained environment (Kraus and Hasiotis, 2006). Kraus (1999) suggested calculating sediment accumulation rates by dividing the thickness of a given stratigraphic section by its known or estimated time span. The calculated life spans of the studied BBS3 and KGS1 paleosols were approximately 2 ka (166 ± 11 to 164 ± 11 ka; Mohammednoor et al., 2024) and 3 ka (148 ± 11 to 145 ± 11 ka; Mohammednoor et al., 2024), respectively, and using their thicknesses, the sedimentation rates are calculated to have been 0.5 and 0.23 mm/yr, respectively, higher than those of the other paleosols. Based on these properties, the BBS3 and KGS1 calcretes are likely to have formed in a proximal floodplain. In BBS2 and KGS3 paleosols, the stage IV and V calcretes indicate mature development, with abundant calcareous root casts in the nodular horizon in BBS2 and few in the nodular horizon in KGS3 reflecting good drainage in BBS2 and poor drainage in KGS3, respectively. The calculated life spans of the studied BBS2 and KGS3 paleosols were 25 ka (212 ± 18 to 187 ± 15 ka; Mohammednoor et al., 2024) and 8 ka (22 ± 3 to ~14 ka; Mohammednoor et al., 2024), respectively, and using their thicknesses, the sedimentation rates are calculated to have been 0.04 and 0.2 mm/yr, respectively. Based on these characteristics, the BBS2 and KGS3 calcretes are likely to have formed more distally in the floodplain than the BBS3 and KGS1 calcretes. In the KGS2 paleosol, well-developed slickensides and blocky peds indicate a vertic horizon and a well-developed paleosol (Retallack, 2019), and the Fe/Mn oxide nodules reflect oxidizing and well-drained conditions (Retallack, 2019). The calculated life span of the studied KGS2 paleosol was 9 ka (123 ± 10-114 ±10 ka; Mohammednoor et al., 2024), and the sedimentation rate is calculated to have been 0.16 mm/yr. Based on these characteristics, similar to the BBS2 and KGS3 calcrete-bearing paleosols, the KGS2 paleosol is likely to have formed more distal in the floodplain than the BBS3 and KGS1 (Fig. 10).

6. Conclusions

Aridisols/Calcisols and Vertisols intercalated in the Pleistocene (~230 to <17 ka) alluvial sediments in the middle Atbara River region in eastern Sudan contain pedogenic carbonates mainly such as calcretes, and disorthic and septaric nodules, respectively. The calcretes partly consist of orthic nodular horizons overlain by laminar horizon, and partly of orthic nodular horizon. Since the pedogenic carbonates studied seem free of inherited carbonates and diagenetic modification, they are most likely well-suited for paleoclimatic analysis. In the study area, an arid to semi-arid climate prevailed during the formation of calcretes in units

BBS and KGS1 during MIS 7-6. Then the climate became more humid during the formation of KGS2 paleosols in MIS 5 to 3, and it finally became drier again during the formation of KGS3 calcrete in MIS 2. The vegetation cover was a mixture of C_3 and C_4 plants with rainfall generally exceeding 350 mm/yr. The well-developed calcretes (stage IV-V) in the BBS2 and KGS3 paleosols (Aridisols) and well-developed vertic horizon in the KGS2 paleosols (Vertisols) formed in distal floodplain settings, whereas the weak-developed calcretes (stage II) in the BBS3 and KGS1 paleosols (Aridisols) formed in proximal floodplain area. Similarities in thickness and morphology of the Pleistocene calcretes in eastern Sudan with Pleistocene calcretes in East Africa indicate similar climatic conditions during their formation. However, the regional climate record reconstructed from different proxies shows that the climatic conditions in the study area were similar to those in East Africa after ~ 70 ka, especially during the LGM. Therefore, further studies of Pleistocene pedogenic carbonates from the terrestrial sedimentary record of the Nile Basin and Sahel region, particularly quantitative climatic reconstructions, are needed to improve continental climatic comparisons. Such studies would lead to a better understanding of the environment of African mammalian evolution, including that of *Homo,* which may have dispersed to Eurasia via the Nile corridor during this time.

Acknowledgements

This study was funded by a PhD scholarship to M. Mohammednoor from the German Academic Exchange Service, Germany (Deutscher Akademischer Austauschdienst, DAAD, Germany, ref. no. 91771155), by grants from the German Research Foundation, Germany (Deutsche Forschungsgemeinschaft, Germany, project 387794796), the National Geographic Society, United States (Explorer’s Grant CP-086R-17), and the European Research Council

(ERC Consolidator Grant, PALEONILE, project 101045217) to F. Bibi. We thank Cordelia Lange and Lorenz Kemmler from Technische Universität Berlin, Germany for assistance with the laboratory work.

References

Abbate, E., Albianelli, A., Awad, A., Billi, P., Bruni, P., Delfino, M., Ferretti, M.P., Filippi, O., Gallai, G., Ghinassi, M., Lauritzen, S.-E., Vetro, D.L., Martínez-Navarro, B., Martini, F., Napoleone, G., Bedri, O., Papini, M., Rook, L., Sagri, M., 2010. Pleistocene environments and human presence in the middle Atbara valley (Khashm El Girba, Eastern Sudan). Palaeogeogr. Palaeoclimatol. Palaeoecol. 292, 12–34. https://doi.org/10.1016/j.palaeo.2010.03.022

Abdelmalik, A.M., Babikir, I.A.A., Ajloon, F.H., Elhag, F.M.A., Ibrahim, I.A., Khatir, A.A., 2024. Production of browse trees/shrubs under climate change conditions in the Butana rangelands of Sudan. J. of Rangel. Sci. 14, 1–9. https://dx.doi.org/10.57647/j.jrs.2024.1402.14

Abell, P.I., Williams, M.A.J., 1989. Oxygen and carbon isotope ratios in gastropod shells as indicators of paleoenvironments in the Afar region of Ethiopia. Palaeogeogr. Palaeoclimatol. Palaeoecol. 74, 265–278. https://doi.org/10.1016/0031-0182(89)90065-5

Alonso-Zarza, A.M., 2003. Palaeoenvironmental significance of palustrine carbonates and calcretes in the geological record. Earth-Sci. Rev. 60, 261–298. https://doi.org/10.1016/S0012-8252(02)00106-X

Alonso-Zarza, A.M., 1999. Initial stages of laminar calcrete formation by roots: examples from the Neogene of central Spain. Sediment. Geol. 126, 177–191. https://doi.org/10.1016/S0037-0738(99)00039-1

Alonso-Zarza, A.M., Silva, P.G., 2002. Quaternary laminar calcretes with bee nests: evidences of small-scale climatic fluctuations, Eastern Canary Islands, Spain. Palaeogeogr. Palaeoclimatol. Palaeoecol. 178, 119–135. https://doi.org/10.1016/S0031-0182(01)00405-9

Alonso-Zarza, A.M., Wright, V.P., 2010. Calcretes, in: Alonso-Zarza, A.M., Tanner, L.H. (Eds.), Carbonates in Continental Settings: Facies, Environment, and Processes. Dev. Sedimentol. 61, Elsevier, pp. 225–267. https:// doi 10.1016/S0070-4571(09)06105-6

Asrat, A., Baker, A., Leng, M.J., Hellstrom, J., Mariethoz, G., Boomer, I., Yu, D., Jex, C.N., Gunn, J., 2018. Paleoclimate change in Ethiopia around the last interglacial derived from annually-resolved stalagmite evidence. Quat. Sci. Rev. 202, 197–210. https://doi.org/10.1016/j.quascirev.2018.06.016

Barker, P.A., Leng, M.J., Gasse, F., Huang, Y., 2007. Century-to-millennial scale climatic variability in Lake Malawi revealed by isotope records. Earth Planet. Sci. Lett. 261, 93–103. https://doi.org/10.1016/j.epsl.2007.06.010

Barrows, T.T., Williams, M.A.J., Mills, S.C., Duller, G.A.T., Fifield, L.K., Haberlah, D., Tims, S.G., Williams, F.M., 2014. A White Nile megalake during the last interglacial period. Geol. 42, 163–166. https:// doi.org/10.1130/G35238.1

Beverly, E., Lukens, W., Stinchcomb, G., 2018. Paleopedology as a tool for reconstructing paleoenvironments and paleoecology: Reconstructing Cenozoic Terrestrial Environments and Ecological Communities, in: Croft, D.A., et al. (Eds.), Vertebrate Paleobiology and Paleoanthropology. Springer International Publishing AG, pp. 151–183. https://doi.org/10.1007/978-3-319-94265-0_9

Blokhuis, W.A., 1993. Vertisols in the Central Clay Plain of the Sudan (PhD dissertation). Agricultural University, Wageningen, pp. 419.

Blokhuis, W.A., Pape, Th., Slager, S., 1969. Morphology and distribution of pedogenic carbonate in some vertisols of the Sudan. Geoderma 2, 173–200. https://doi.org/10.1016/0016-7061(69)90037-8

Bullock, P., Fedoroff, N., Jongerius, A., Stoops, G., Tursina, T., 1985. Handbook for Soil Thin Section Description. Waine Research Publications, Wolverhampton, pp. 152.

Buursink, J., 1971. Soil of Central Sudan (PhD dissertation). Rijksuniversiteit te Utrecht, Utrecht, pp. 450.

Candy, I., Black, S., Sellwood, B.W., 2004. Quantifying time scales of pedogenic calcrete formation using U-series disequilibria. Sediment. Geol. 170, 177–187. https://doi.org/10.1016/j.sedgeo.2004.07.003

Cerling, T.E., 1984. The stable isotopic composition of modern soil carbonate and its relationship to climate. Earth Planet. Sci. Lett. 71, 229–240. https://doi.org/10.1016/0012-821X(84)90089-X

Cerling, T.E., Harris, J.M., MacFadden, B.J., Leakey, M.G., Quade, J., Eisenmann, V., Ehleringer, J.R., 1997. Global vegetation change through the Miocene/Pliocene boundary. Nat. 389, 153–158. http://dx.doi.org/10.1038/38229

Cerling, T.E., Hay, R.L., 1986. An isotopic study of paleosol carbonates from Olduvai Gorge. Quat. Res. 25, 63–78. https://doi.org/doi:10.1016/0033-5894(86)90044-X

Cerling, T.E., Hay, R.L., O'Neil, J.R., 1977. Isotopic evidence for dramatic climatic changes in East Africa during the Pleistocene. Nat. 267, 137–138. https://doi.org/10.1038/267137a0

Cerling, T.E., Quade, J., 1993. Stable carbon and oxygen isotopes in soil carbonates, in: Swart, P.K., et al. (Eds.), Climate Change in Continental Isotopic Records. Geophys. Monogr. Ser., pp. 217–231. https://doi.org/10.1029/GM078p0217

Cerling, T.E., Wynn, J.G., Andanje, S.A., Bird, M.I., Korir, D.K., Levin, N.E., Mace, W., Macharia, A.N., Quade, J., Remien, C.H., 2011. Woody cover and hominin environments in the past 6 million years. Nat. 476, 51–56. https://doi.org/doi:10.1038/nature10306

Cohen, A.S., Stone, J.R., Beuning, K.R.M., Park, L.E., Reinthal, P.N., Dettman. D., Scholz, C.A., Johnson, T.C., King, J.W., Talbot, M.R., Brown, E.T., Ivory, S.J., 2007. Ecological consequences of early Late Pleistocene megadroughts in tropical Africa. Proc. Natl. Acad. Sci. 104, 16422–16427. https://doi.org/10.1073/pnas.0703873104

Cohen, K.M., Gibbard, P.L., 2019. Global chronostratigraphical correlation table for the last 2.7 million years, version 2019 Q1-500. Quat. Int. 500, 20–31. https://doi.org/10.1016/j.quaint.2019.03.009

Costa, K., Russell, J., Konecky, B., Lamb, H., 2014. Isotopic reconstruction of the African Humid Period and Congo Air Boundary migration at Lake Tana, Ethiopia. Quat. Sci. Rev. 83, 58–67. https://doi.org/10.1016/j.quascirev.2013.10.031

Crosta, X., Romero, O.E., Ther, O., Schneider, R.R., 2012. Climatically-controlled siliceous productivity in the eastern Gulf of Guinea during the last 40 000 yr. Clim. Past 8, 415–431. https://doi.org/10.5194/cp-8-415-2012

Dawelbeit, A., Jaillard, E., Eisawi, A., 2019. Sedimentary and paleobiological records of the latest Pleistocene-Holocene climate evolution in the Kordofan region, Sudan. J. Afr. Earth Sci. 160, 103605. https://doi.org/10.1016/j.jafrearsci.2019.103605

Durand, N., Monger, H.C., Canti, M.G., Verrecchia, E.P., 2018. Calcium carbonate features, in: Stoops, G., Marcelino, V., Mees, F. (Eds.), Interpretation of Micromorphological Features of Soils and Regoliths. Elsevier, pp. 205–258.

Eisawi, A., Schrank, E., 2009. Terrestrial palynology and age assessment of the Gedaref Formation (eastern Sudan). J. Afr. Earth Sci. 54, 22–30. https://doi.org/10.1016/j.jafrearsci.2009.01.005

Esteban, M., Klappa, C.F., 1983. Subaerial exposure environments, in: Scholle, P.A., Bebout, D.G., Moore, C.H. (Eds.), Carbonate Depositional Environments. Am. Assoc. Pet. Geol. Mem., pp. 1–96.

Fedoroff, N., Courty, M.A., Guo, Z., 2018. Palaeosoils and relict soils: A conceptual approach, in: Stoops, G., Marcelino, V., Mees, F. (Eds.), Interpretation of Micromorphological Features of Soils and Regoliths. Elsevier, Netherlands, pp. 821-862.

Felske, G.N., 2016. Genesis of Calcrete and Related Carbonate Rocks in the Southern Kenya Rift (Thesis of Master). University of Saskatchewan, Saskatoon, pp. 168.

Felton, A.A., Russell, J.M., Cohen, A.S., Baker, M.E., Chesley, J.T., Lezzar, K.E., McGlue, M.M., Pigati, J.S., Quade, J., Stager, J.C., Tiercelin, J.J., 2007. Paleolimnological evidence for the onset and termination of glacial aridity from Lake Tanganyika, Tropical East Africa. Palaeogeogr. Palaeoclimatol. Palaeoecol. 252, 405–423. https://doi.org/10.1016/j.palaeo.2007.04.003

Foerster, V., Asrat, A., Bronk Ramsey, C., Brown, E.T., Chapot, M.S., Deino, A., Duesing, W., Grove, M., Hahn, A., Junginger, A., Kaboth-Bahr, S., Lane, C.S., Opitz, S., Noren, A., Roberts, H.M., Stockhecke, M., Tiedemann, R., Vidal, C.M., Vogelsang, R., Cohen, A.S., Lamb, H.F., Schaebitz, F., Trauth, M.H., 2022. Pleistocene climate variability in Eastern Africa influenced hominin evolution. Nat. Geosci. 15, 805–811. https://doi.org/10.1038/s41561-022-01032-y

Fox, D.L., Koch, P.L., 2003. Tertiary history of C4 biomass in the Great Plains, USA. Geol. 31, 809–812. https://doi.org/doi: https://doi.org/10.1130/G19580.1

Frédoux, A., 1994. Pollen analysis of a deep-sea core in the Gulf of Guinea: vegetation and climatic changes during the last 225,000 years B.P. Palaeogeogr. Palaeoclimatol. Palaeoecol. 109, 317–330. https://doi.org/10.1016/0031-0182(94)90182-1

Gile, L.H., Peterson, F.F., Grossman, R.B., 1966. Morphological and genetic sequences of carbonate accumulation in desert soils. Soil Sci. 101, 347–360.

Goldsmith, J.R., Graf, D.L., Heard, H.C., 1961. Lattice constants of the calcium-magnesium carbonates. Am. Miner. 46, 453–457.

Gosling, W.D., Miller, C.S., Shanahan, T.M., Holden, P.B., Overpeck, J.T., van Langevelde, F., 2022. A stronger role for long-term moisture change than for CO_2 in determining tropical woody vegetation change. Sci. 376, 653–656. https://doi. org/10.1126/science.abg4618

Goudie, A.S., 1983. Calcrete, in: Goudie, A.S., Pye, K. (Eds.), Chemical Sediments and Geomorphology. Academic Press, London, New York, pp. 93–131.

Gupta, P., Noone, D., Galewsky, J., Sweeney, C., Vaughn, B.H., 2009. Demonstration of high-precision continuous measurements of water vapor isotopologues in laboratory and remote field deployments using wavelength-scanned cavity ring-down spectroscopy (WS-CRDS) technology. Rapid Commun. Mass Spectrom. 23, 2534–2542. https://doi.org/10.1002/rcm.4100

Hardy, R.G., Tucker, M.E., 1988. X-ray powder diffraction of sediments, In: Tucker, M.E. (Ed.), Techniques in Sedimentology. Blackwell Science Publishers, pp. 91–228.

Harrison, M.N., Jackson, J.K., 1958. Ecological Classification of the Vegetation of the Sudan. Ministry of Agriculture, Sudan, pp. 45.

Hawley, J.H., Bachman, G.O., Manley, K., 1976. Quaternary stratigraphy in the Basin and Range and Great Plains provinces, New Mexico and western Texas, in: Mahaney, W.C. (Ed.), Quaternary Stratigraphy of North America. Dowden, Hutchinson, and Ross, Stroudsburg, Pa., pp. 235–274.

Hay, R.L., Reeder, R.L., 1978. Calcretes of Olduvai Gorge and the Ndolanya Beds of northern Tanzania. Sedimentol. 25, 649–673. https://doi.org/10.1111/j.1365-3091.1978.tb00324.x

Hillaire-Marcel, C., Carro, O., Casanova, J., 1986. ^{14}C and Th/U dating of Pleistocene and Holocene stromatolites from East Africa paleolakes. Quat. Res. 25, 312–329. https://doi.org/10.1016/0033-5894(86)90004-9

Horn, B.L.D., Pereira, V.P., Schultz, C.L., 2013. Calcretes of the Santa Maria Supersequence, Middle Triassic, Rio Grande do Sul, Brazil: Classification, genesis and paleoclimatic implications. Palaeogeogr. Palaeoclimatol. Palaeoecol. 376, 39–47. https://doi.org/10.1016/j.palaeo.2013.02.013

Jarraya, F., Rogerson, M., Kallel, N., Mauz, B., Elmejdoub, N., Sghari, A., 2024. Environmental and climatic significance of the Pliocene-Pleistocene calcretes in North Africa. Catena 244, 108236. https://doi.org/10.1016/j.catena.2024.108236

Kallweit, W., Mollenhauer, G., Zabel, M., 2012. Multi-proxy reconstruction of terrigenous input and sea-surface temperatures in the eastern Gulf of Guinea over the last ~35 ka. Mar. Geol. 319–322, 35–46. https://doi.org/10.1016/j.margeo.2012.06.007

Kaplan, M.Y., Eren, M., Kadir, S., Kapur, S., 2013. Mineralogical, geochemical and isotopic characteristics of Quaternary calcretes in the Adana region, southern Turkey: Implications on their origin. Catena 101, 164–177. https://doi.org/10.1016/j.catena.2012.09.004

Khalaf, F.I., Al-Zamel, A., 2016. Petrography, micromorphology and genesis of Holocene pedogenic calcrete in Al-Jabal Al-Akhdar, Sultanate of Oman. Catena 147, 496–510. https://doi.org/10.1016/j.catena.2016.07.044

Kim, S.-T., O'Neil, J.R., 1997. Equilibrium and nonequilibrium oxygen isotope effects in synthetic carbonates. Geochim. Cosmochim. Acta 61, 3461–3475. https://doi.org/10.1016/S0016-7037(97)00169-5

Klappa, C.F., 1980. Rhizoliths in terrestrial carbonates: classification, recognition, genesis and significance. Sedimentol. 27, 613–629. https://doi.org/10.1111/j.1365-3091.1980.tb01651.x

Kovda, I., Mermut, A.R., 2018. Vertic features, in: Stoops, G., Marcelino, V., Mees, F. (Eds.), Interpretation of Micromorphological Features of Soils and Regoliths. Elsevier, pp. 605–632.

Kraus, M.J., 1999. Paleosols in clastic sedimentary rocks: their geologic applications. Earth-Sci. Rev. 47, 41–70. https://doi.org/10.1016/S0012-8252(99)00026-4

Kraus, M.J., Hasiotis, S., 2006. Significance of different modes of rhizolith preservation to interpreting paleoenvironmental and paleohydrologic settings: Examples from Paleogene paleosols, Bighorn Basin, Wyoming, U.S.A. J. Sediment. Res. 76, 633–646. https://doi.org/10.2110/jsr.2006.052

Lamb, H.F., Bates, C.R., Bryant, C.L., Davies, S.J., Huws, D.G., Marshall, M.H., Roberts, H.M., Toland, H., 2018. 150,000-year palaeoclimate record from northern Ethiopia supports early, multiple dispersals of modern humans from Africa. Sci. Rep. 8, 1077. https:// doi.org/10.1038/s41598-018-19601-w

Lamb, H.F., Bates, C.R., Coombes, P.V., Marshall, M.H., Umer, M., Davies, S.J., Dejen, E., 2007. Late Pleistocene desiccation of Lake Tana, source of the Blue Nile. Quat. Sci. Rev. 26, 287-299. https://doi.org/10.1016/j.quascirev.2006.11.020

Leeder, M.R., 1975. Pedogenic carbonates and flood sediment accretion rates: a quantitative model for alluvial arid-zone lithofacies. Geol. Mag. 112, 257–270. https://doi.org/10.1017/S0016756800047014

Leplongeon, A., 2021. The Main Nile Valley at the end of the Pleistocene (28–15 ka): Dispersal corridor or environmental refugium? Front. Earth Sci. 8, 607183. https://doi.org/10.3389/feart.2020.607183

Levin, N.E., Brown, F.H., Behrensmeyer, A.K., Bobe, R., Cerling, T.E., 2011. Paleosol carbonates from the Omo Group: Isotopic records of local and regional environmental change in East

Africa. Palaeogeogr. Palaeoclimatol. Palaeoecol. 307, 75–89. https://doi.org/10.1016/j.palaeo.2011.04.026

Machette, M.N., 1985. Calcic soils of the southwestern United States, in: Weide, D.L. (Ed.), Soils and Quaternary Geology of the Southwestern United States. Geol. Soc. Am., pp. 1–21. https://doi.org/10.1130/SPE203-p1

Marret, F., Kim, S-Y., Scourse, J., 2013. A 30,000 yr record of land–ocean interaction in the eastern Gulf of Guinea. Quat. Res. 80, 1–8. http://dx.doi.org/10.1016/j.yqres.2013.04.003

Mermut, A.R., Dasog, G.S., Dowuona, G.N., 1996. Soil morphology, in: Ahmad, N., Mermut, A. (Eds.), Vertisols and Technologies for Their Management. Dev. Soil Sci. 24, Elsevier, Amsterdam, pp. 89–114.

Mirghani, M., 2002. Concepts and Models for the Characterization of the West Gedaref Hydrogeologic System, Sudan (PhD dissertation). Technische Universität Berlin, Berlin, pp. 123.

Moernaut, J., Verschuren, D., Charlet, F., Kristen, I., Fagot, M., De Batist, M., 2010. The seismic-stratigraphic record of lake-level fluctuations in Lake Challa: Hydrological stability and change in equatorial East Africa over the last 140 kyr. Earth Planet. Sci. Lett. 290, 214–223. http://dx.doi.org/10.1016/j.epsl.2009.12.023

Mohammednoor, M., Bibi, F., Eisawi, A., Tsukamoto, S., Bussert, R., 2024. Quaternary alluvial paleosols of the Atbara River, eastern Sudan: description and paleoenvironments. J. Quat. Sci. 39, 102–118. https://doi.org/10.1002/jqs.3574

Müller, G., Gastner, M., 1971. The "Karbonat-Bombe", a simple device for the determination of the carbonate content in sediments, soils and other minerlas. Neues Jahrb. für Mineral. 10, 466–469.

Netterberg, F., 1980. Geology of southern African calcretes: 1: Terminology, description, macrofeatures, and classification. South Afr. J. Geol. 83, 255–283.

Netterberg, F., 1969. The Geology and Engineering Properties of South African Calcretes (PhD dissertation). University of Witwatersrand, Johannesburg, pp. 1070.

O'Neil, J.R., Clayton, R.N., Mayeda, T.K., 1969. Oxygen isotope fractionation in divalent metal carbonates. J. Chem. Phys. 51, 5547–5558. https://doi.org/10.1063/1.1671982

Owen, R.B., Renaut, R.W., Behrensmeyer, A.K., Potts, R., 2014. Quaternary geochemical stratigraphy of the Kedong–Olorgesailie section of the southern Kenya Rift valley. Palaeogeogr. Palaeoclimatol. Palaeoecol. 396, 194–212. https://doi.org/10.1016/j.palaeo.2014.01.011

Retallack, G.J., 2019. Soils of the Past: An Introduction to Paleopedology, Third Edition. John Wiley and Sons, Ltd, Hoboken, USA, pp. 534.

Richoz, S., Baldermann, A., Frauwallner, A., Harzhauser, M., Daxner-Höck, G., Klammer, D., Piller, W.E., 2017. Geochemistry and mineralogy of the Oligo-Miocene sediments of the Valley of Lakes, Mongolia. Palaeobiodivers. Palaeoenviron. 97, 233–258. https://doi.org/DOI 10.1007/s12549-016-0268-6

Rodrigues, A.G., Dal' Bo´, P.F., Basilici, G., Soares, M.V.T., Menezes, M.N., 2019. Biotic influence in the genesis of laminar calcretes in Vertisols of the Marília Formation (Upper Cretaceous, Brazil). J. Sediment. Res. 89, 440–458. https://doi.org/10.2110/jsr.2019.22

Sasso, G.D., Zerboni, A., Maritan, L., Angelini, I., Compostella, C., Usai, D., Artioli, G., 2018. Radiocarbon dating reveals the timing of formation and development of pedogenic calcium carbonate concretions in Central Sudan during the Holocene. Geochim. Cosmochim. Acta 238, 16–35. https://doi.org/10.1016/j.gca.2018.06.037

Schaetzl, R.J., Thompson, M., 2015. Soils Genesis and Geomorphology, Second Edition. Cambridge University Press, Cambridge, pp. 817.

Scholz, C.A., Johnson, T.C., Cohen, A.S., King, J.W., Peck, J.A., Overpeck, J.T., Talbot, M.R., Brown, E.T., Kalindekafe, L., Amoako, P.Y.O., Lyons, R.P., Shanahan, T.M., Castaneda, I.S., Heil, C.W., Forman, S.L., McHargue, L.R., Beuning, R.K., Gomez, J., Pierson, J., 2007. East African megadroughts between 135 and 75 thousand years ago and bearing on early-modern human origins. Proc. Natl. Acad. Sci. 104, 16416–16421. https://doi.org/10.1073/pnas.0703874104

Soil Survey Staff, 2017. Soil Survey Manual, Fourth Edition. Handbook U.S. Department of Agriculture, Washington DC, pp. 603.

Srivastava, A.K., Bansod, M.N., Singh, A., Sharma, N., 2019. Geochemistry of paleosols and calcretes from Quaternary sediments of Purna alluvial basin, central India: An emphasis on paleoclimate. Rhizosphere 11, 100162. https://doi.org/10.1016/j.rhisph.2019.100162

Stone, J.R., Westover, K.S., Cohen, A.S., 2011. Late Pleistocene paleohydrography and diatom paleoecology of the central basin of Lake Malawi, Africa. Palaeogeogr. Palaeoclimatol. Palaeoecol. 303, 51–70. http://dx.doi.org/10.1016/j.palaeo.2010.01.012

Stoops, G., 2021. Guidelines for Analysis and Description of Soil and Regolith Thin Sections, Second Edition. Wiley. pp. 256.

Stoops, G., 2003. Thin Section Preparation of Soils and Sediments. Soil Science Society of America, Madison, pp. 185.

Stoops, G., Marcelino, V., 2018. Lateritic and bauxitic materials, in: Stoops, G., Marcelino, V., Mees, F. (Eds.), Interpretation of Micromorphological Features of Soils and Regoliths. Elsevier, Netherlands, pp. 691–720.

Stoops, G., Marcelino, V., Mees, F., 2018. Micromorphological features and their relation to processes and classification: General guidelines and keys, in: Stoops, G., Marcelino, V., Mees, F. (Eds.), Interpretation of Micromorphological Features of Soils and Regoliths. Elsevier, Netherlands, pp. 895–917.

Tabor, N.J., Hope Jahren, A., Wyman, L., Feseha, M., Todd, L., Kappleman, J., 2021. Stable isotope geochemistry of the modern Shinfa River, northwestern Ethiopian lowlands: a potential model for interpreting ancient environments of the Middle Stone Age, in: Bojar, A.-V., Pelc, A., Lecuyer, C. (Eds.), Stable Isotope Studies of the Water Cycle and Terrestrial Environments. Geol. Soc. London, pp. 225-253.

Tabor, N.J., Myers, T.S., Michel, L.A., 2017. Sedimentologist’s guide for recognition, description, and classification of paleosols, in: Zeigler, K.E., Parker, W.G. (Eds.), Terrestrial Depositional Systems. Elsevier, pp. 165–208. https://doi.org/10.1016/B978-0-12-803243-5.00004-2

Talma, A.S., Netterberg, F., 1983. Stable isotope abundances in calcretes, in: Wilson, R.C.L. (Ed.), Residual Deposits: Surface Related Weathering Processes and Materials. Geol. Soc. London, Blackwell, Oxford, pp. 221–233.

Tandon, S.K., Andrews, J.E., 2001. Lithofacies associations and stable isotopes of palustrine and calcrete carbonates: examples from an Indian Maastrichtian regolith. Sedimentol. 48, 339–355. https://doi.org/10.1046/j.1365-3091.2001.00367.x

Tsukamoto, S., Bussert, R., Delagnes, A., Richter, M., Mohammednoor, M., Bedri, O., Kraatz, B., Müller, J., Salih, K., Eisawi, A., Bibi, F., 2022. Luminescence chronology of fossiliferous fluvial sediments along the middle Atbara River, Sudan. Quat. Geochronol. 71, 101312. https://doi.org/10.1016/j.quageo.2022.101312

Vail, J.R., 1988. Lexicon of the Geological Terms for the Sudan. A.A. Balkema, Rotterdam, pp. 199.

Valera-Fernández, D., Cabadas-Báez, H., Solleiro-Rebolledo, E., Landa-Arreguín, F.J., Sedov, S., 2020. Pedogenic carbonate crusts (calcretes) in karstic landscapes as archives for paleoenvironmental reconstructions – A case study from Yucatan Peninsula, Mexico. Catena 194, 104635. https://doi.org/10.1016/j.catena.2020.104635

Vepraskas, M.J., Lindbo, D.L., Stolt, M.H., 2018. Redoximorphic features, in: Stoops, G., Marcelino, V., Mees, F. (Eds.), Interpretation of Micromorphological Features of Soils and Regoliths. Elsevier, Netherlands, pp. 425-445.

Verrecchia, E.P., Trombino, L., 2021. A Visual Atlas for Soil Micromorphologists. Springer, pp. 184.

Wieder, M., Yaalon, D., 1974. Effect of matrix composition on carbonate nodule crystallization. Geoderma 11, 95–121.

Williams, M., 2019. The Nile Basin: Quaternary Geology, Geomorphology and Prehistoric Environments, Third Edition. Cambridge University Press, Cambridge, pp. 426.

Williams, M.A.J., Duller, G.A.T., Williams, F.M., Woodward, J.C., Macklin, M.G., El Tom, O.A.M., Munro, R.N., El Hajaz, Y., Barrows, T.T., 2015. Causal links between Nile floods and Eastern Mediterranean sapropel formation during the past 125 kyr confirmed by OSL and radiocarbon dating of Blue and White Nile sediments. Quat. Sci. Rev., 130, 89–108. https://doi.org/10.1016/j.quascirev.2015. 05.024

Wright, V.P., 2007. Calcrete, in: Nash, D.J., McLaren, S.J. (Eds.), Geochemical Sediments and Landscapes. Blackwell Publishing Ltd, pp. 10–45.

Wright, V.P., 1990a. A micromorphological classification of fossil and recent calcic and petrocalcic microstructures, in: Douglas, L.A. (Ed.), Soil Micro-Morphology: A Basic and Applied Science. Dev. Soil Sci., 19, Elsevier, pp. 401–407. https://doi.org/10.1016/S0166-2481(08)70354-4

Wright, V.P., 1990b. Estimating rates of calcrete formation and sediment accretion in ancient alluvial deposits. Geol. Mag. 127, 273–276. https://doi.org/10.1017/S0016756800014539

Wright, V.P., Platt, N.H., Marriott, S.B., Beck, V.H., 1995. A classification of rhizogenic (root-formed) calcretes, with examples from the Upper Jurassic-Lower Cretaceous of Spain and Upper Cretaceous of southern France. Sediment. Geol. 100, 143–158. https://doi.org/10.1016/0037-0738(95)00105-0.

Wright, V.P., Tucker, M.E., 1991. Calcretes: An Introduction, in: Wright, V.P., Tucker, M.E. (Eds.), Calcretes. Int. Assoc. Sedimentol. Blackwell, pp. 1–22.

Zamanian, K., Pustovoytov, K., Kuzyakov, Y., 2016. Pedogenic carbonates: Forms and formation processes. Earth-Sci. Rev. 157, 1–17. https://doi.org/10.1016/j.earscirev.2016.03.003

Zhou, J., Chafetz, H.S., 2010. Pedogenic carbonates in Texas: Stable-isotope distributions and their implications for reconstructing region-wide paleoenvironments. J. Sediment. Res. 80, 137–150. https://doi.org/10.2110/jsr.2010.018

Zhou, J., Chafetz, H.S., 2009. Biogenic caliches in Texas: The role of organisms and effect of climate. Sediment. Geol. 222, 207–225. https://doi.org/10.1016/j.sedgeo.2009.09.003

Fig. 1

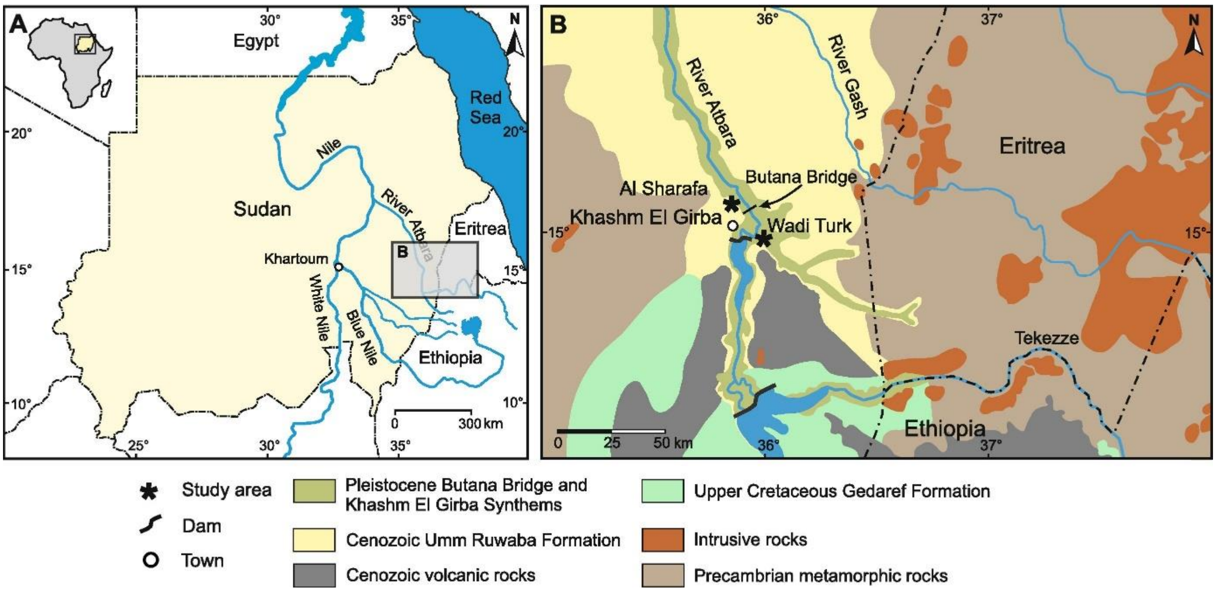
A
Egypt
Red Sea
Sudan
Nile
River Atbara
Eritrea
Khartoum
White Nile
Blue Nile
Ethiopia
0
300 km
30°
35°
20°
15°
10°
25°
N
B
River Atbara
River Gash
Eritrea
Al Sharafa
Butana Bridge
Khashm El Girba
Wadi Turk
Tekezze
Ethiopia
36°
37°
15°
0
25
50 km
N
Study area
Dam
Town
Pleistocene Butana Bridge and Khashm El Girba Synthems
Cenozoic Umm Ruwaba Formation
Cenozoic volcanic rocks
Upper Cretaceous Gedaref Formation
Intrusive rocks
Precambrian metamorphic rocks

Fig. 2

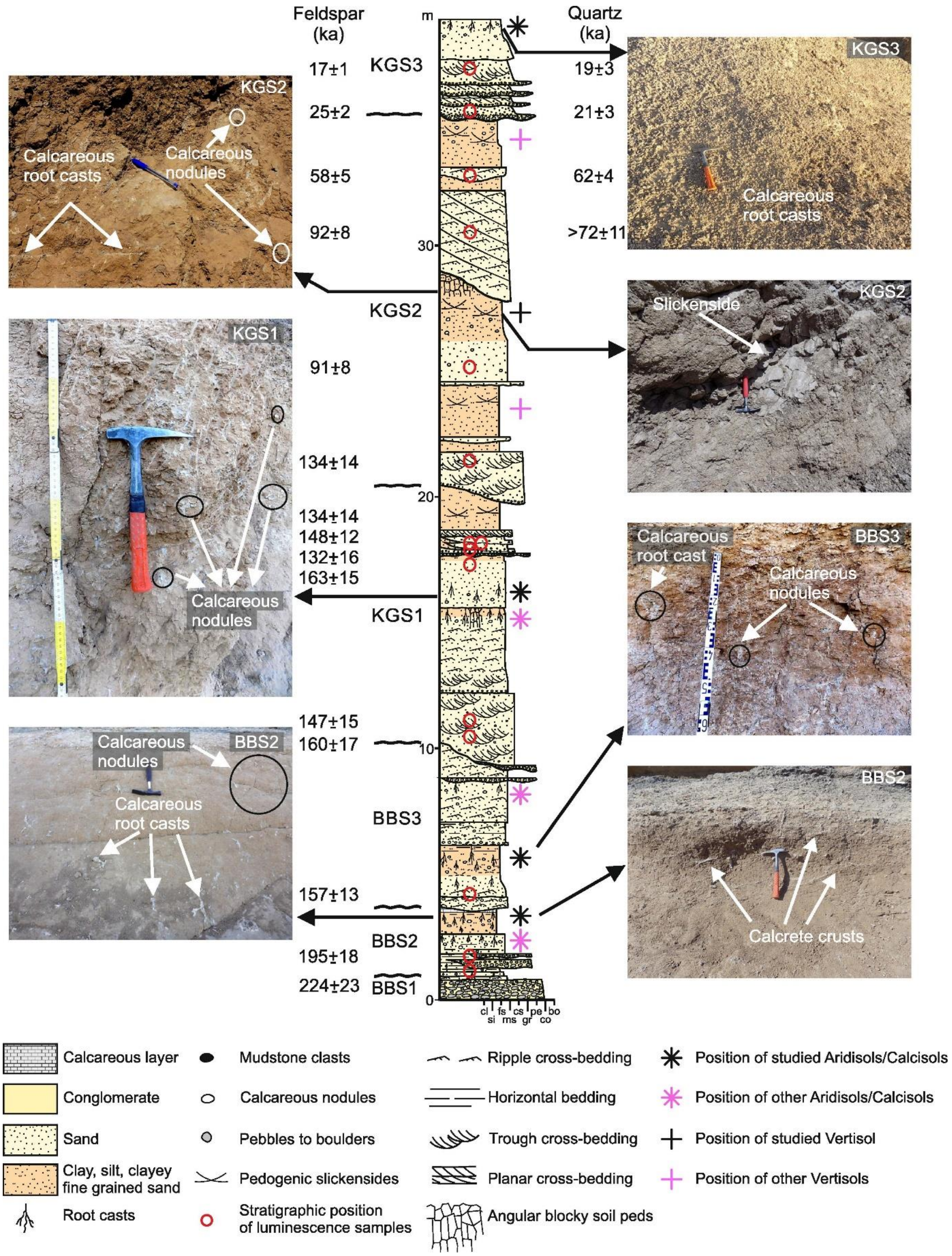

Feldspar (ka)
Quartz (ka)
m
17±1
KGS3
19±3
25±2
21±3
58±5
62±4
92±8
>72±11
30
KGS2
91±8
134±14
20
134±14
148±12
132±16
163±15
KGS1
147±15
160±17
10
BBS3
157±13
BBS2
195±18
224±23
BBS1
0
cl fs cs pe bo
si ms gr co
KGS2
Calcareous root casts
Calcareous nodules
KGS3
Calcareous root casts
KGS2
Slickenside
KGS1
Calcareous nodules
BBS3
Calcareous root cast
Calcareous nodules
BBS2
Calcareous nodules
Calcareous root casts
BBS2
Calcrete crusts
Calcareous layer
Conglomerate
Sand
Clay, silt, clayey fine grained sand
Root casts
Mudstone clasts
Calcareous nodules
Pebbles to boulders
Pedogenic slickensides
Stratigraphic position of luminescence samples
Ripple cross-bedding
Horizontal bedding
Trough cross-bedding
Planar cross-bedding
Angular blocky soil peds
Position of studied Aridisols/Calcisols
Position of other Aridisols/Calcisols
Position of studied Vertisol
Position of other Vertisols

1096 Fig. 3

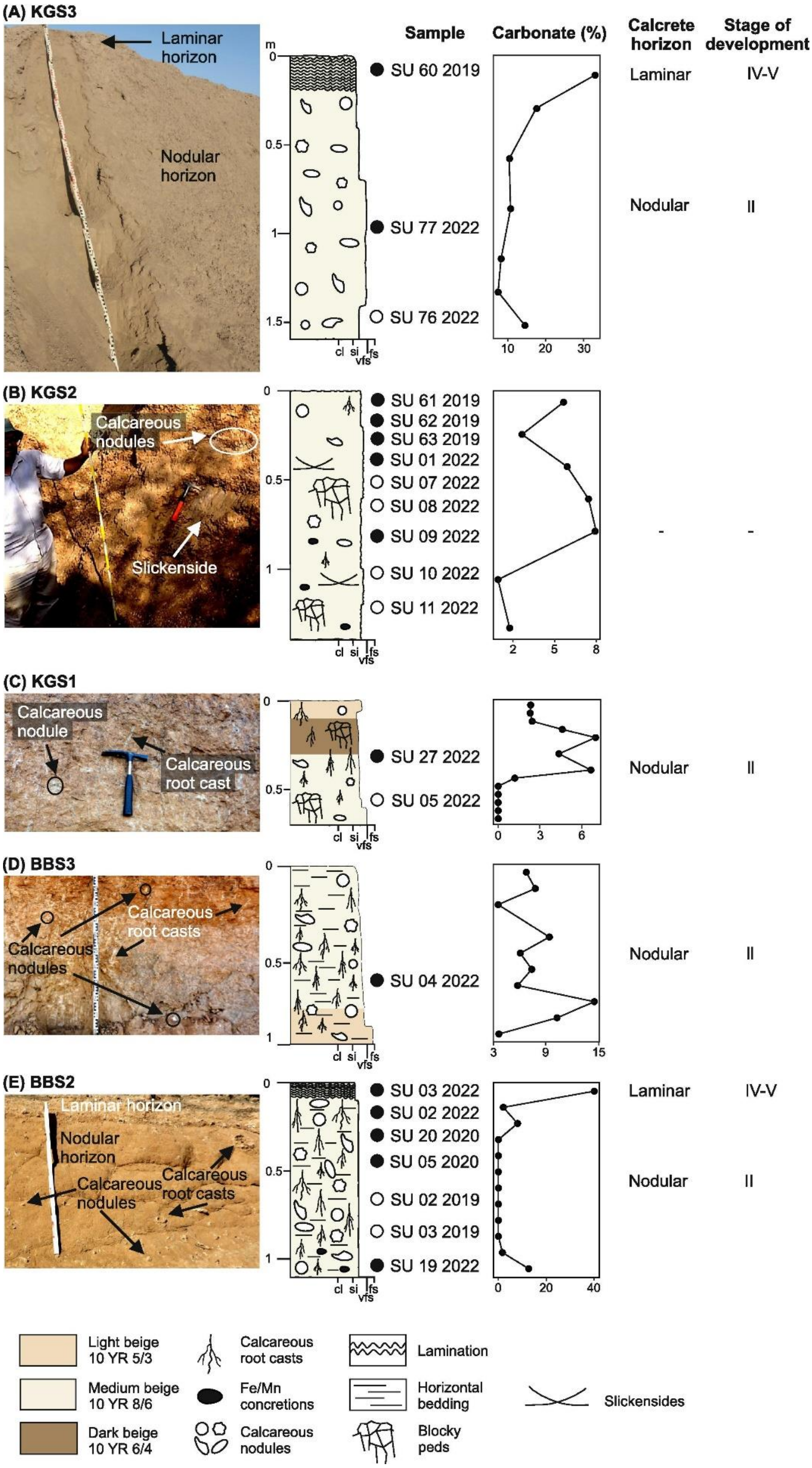

1097

Fig. 4

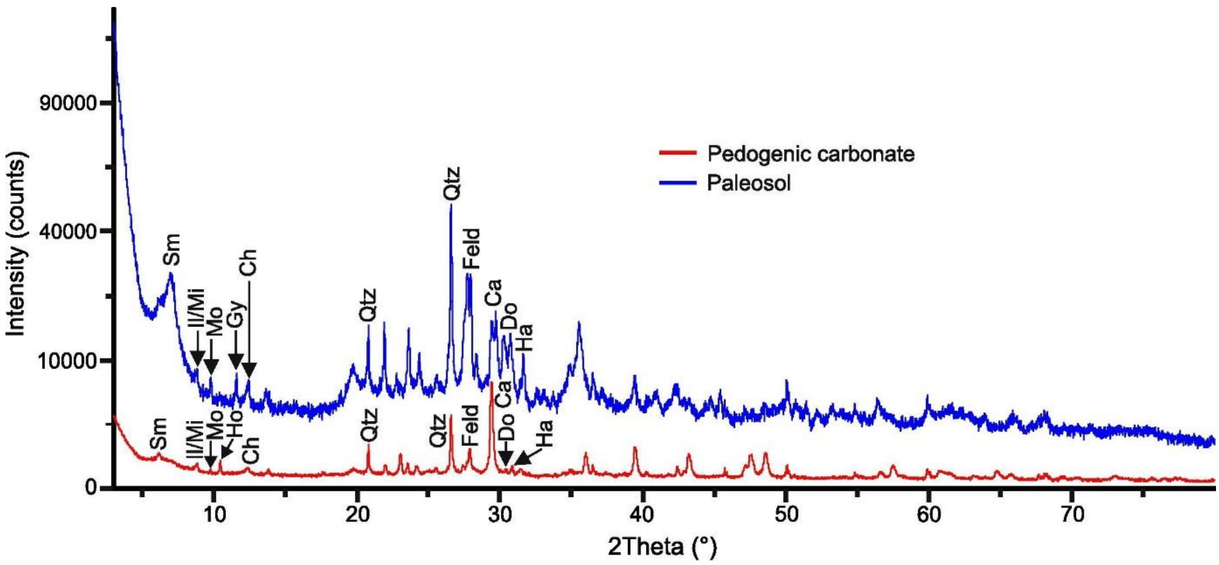

Pedogenic carbonate
Paleosol
Intensity (counts)
2Theta (°)
90000
40000
10000
0
10
20
30
40
50
60
70
Sm
Il/Mi
Mo
Gy
Ch
Qtz
Qtz
Feld
Ca
Do
Ha
Sm
Il/Mi
Mo
Ho
Ch
Qtz
Qtz
Feld
Ca
Do
Ha

Fig. 5

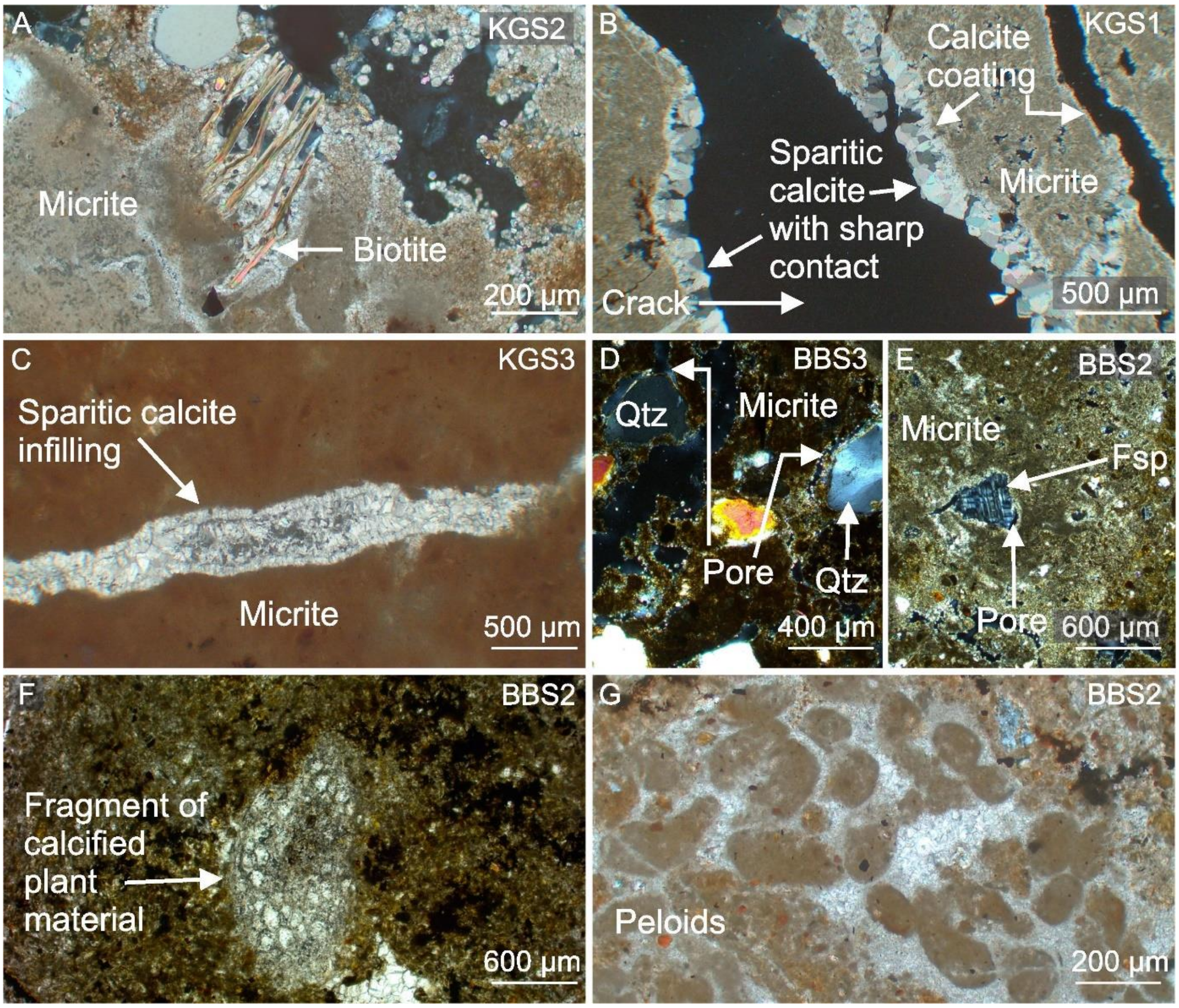
A
KGS2
Micrite
Biotite
200 µm
B
KGS1
Calcite coating
Sparitic calcite with sharp contact
Micrite
Crack
500 µm
C
KGS3
Sparitic calcite infilling
Micrite
500 µm
D
BBS3
Qtz
Micrite
Pore
Qtz
400 µm
E
BBS2
Micrite
Fsp
Pore
600 µm
F
BBS2
Fragment of calcified plant material
600 µm
G
BBS2
Peloids
200 µm

Fig. 6

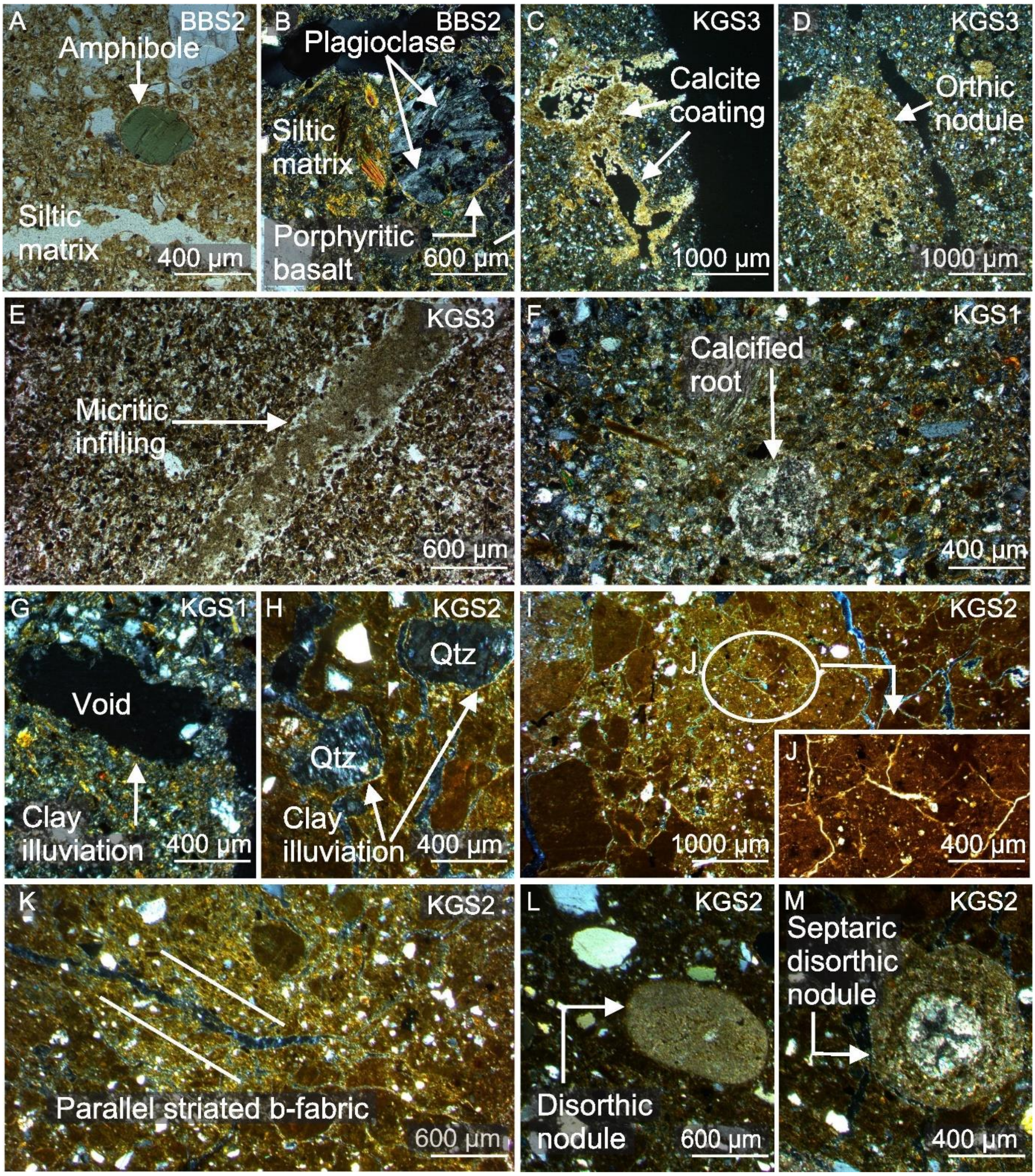

A
BBS2
Amphibole
Siltic matrix
400 µm
B
BBS2
Plagioclase
Siltic matrix
Porphyritic basalt
600 µm
C
KGS3
Calcite coating
1000 µm
D
KGS3
Orthic nodule
1000 µm
E
KGS3
Micritic infilling
600 µm
F
KGS1
Calcified root
400 µm
G
KGS1
Void
Clay illuviation
400 µm
H
KGS2
Qtz
Qtz
Clay illuviation
400 µm
I
KGS2
J
1000 µm
J
400 µm
K
KGS2
Parallel striated b-fabric
600 µm
L
KGS2
Disorthic nodule
600 µm
M
KGS2
Septaric disorthic nodule
400 µm

Fig. 7

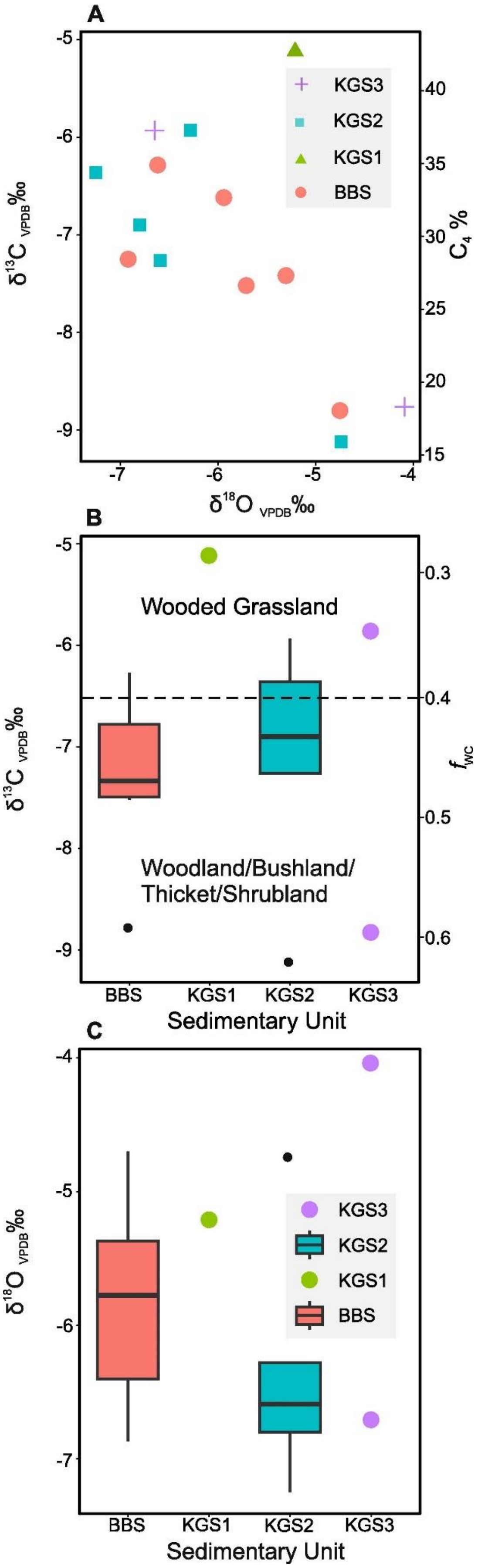
A
KGS3
KGS2
KGS1
BBS
δ13C VPDB‰
δ18O VPDB‰
C4 %
-5
-6
-7
-8
-9
-7
-6
-5
-4
40
35
30
25
20
15
B
Wooded Grassland
Woodland/Bushland/
Thicket/Shrubland
δ13C VPDB‰
fWC
0.3
0.4
0.5
0.6
BBS
KGS1
KGS2
KGS3
Sedimentary Unit
C
δ18O VPDB‰
-4
-5
-6
-7
KGS3
KGS2
KGS1
BBS
BBS
KGS1
KGS2
KGS3
Sedimentary Unit

Fig. 8

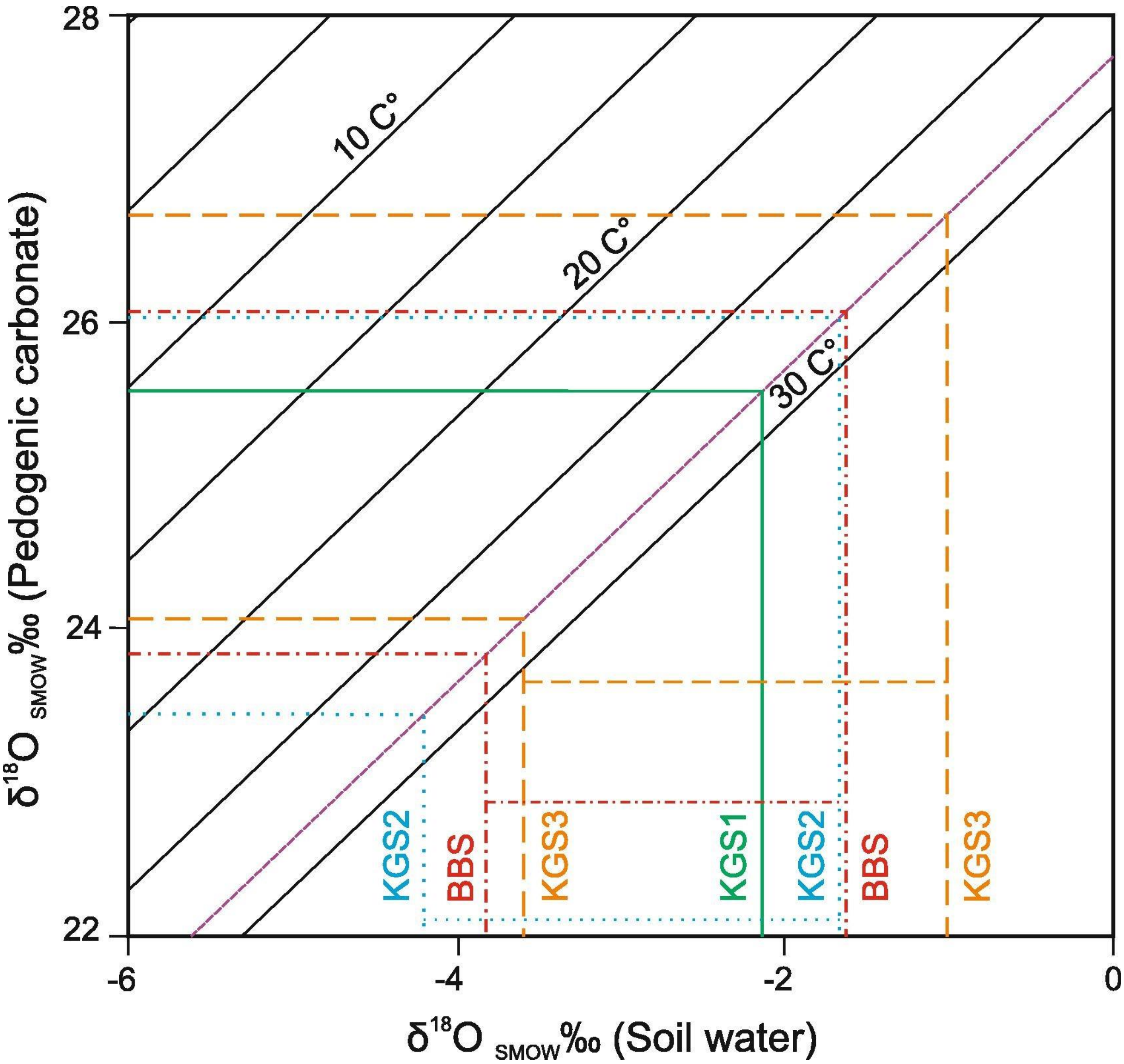

28
26
24
22
-6
-4
-2
0
10 C°
20 C°
30 C°
KGS2
BBS
KGS3
KGS1
KGS2
BBS
KGS3
δ18O SMOW‰ (Pedogenic carbonate)
δ18O SMOW‰ (Soil water)

1108 Fig. 9

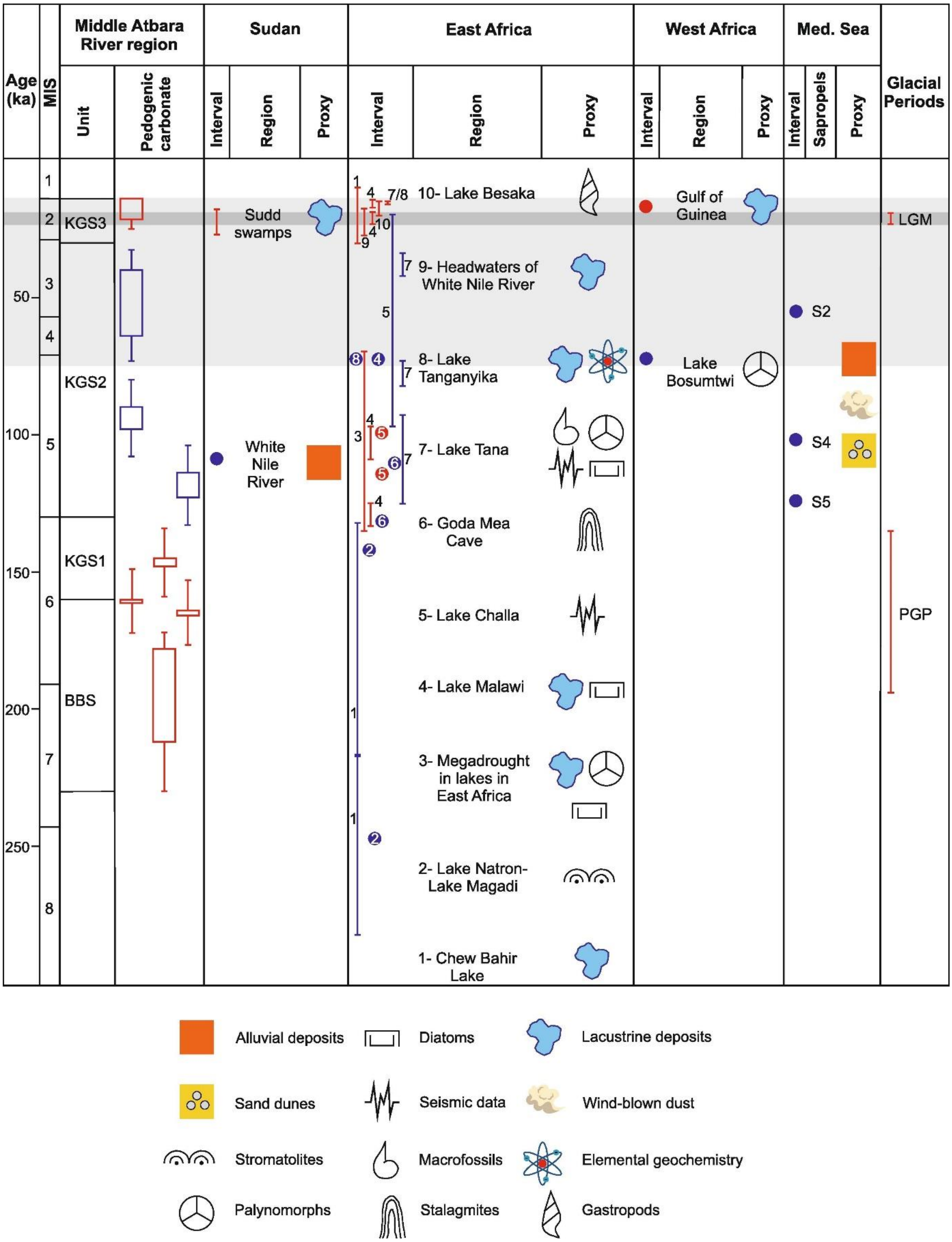

1109

Fig. 10

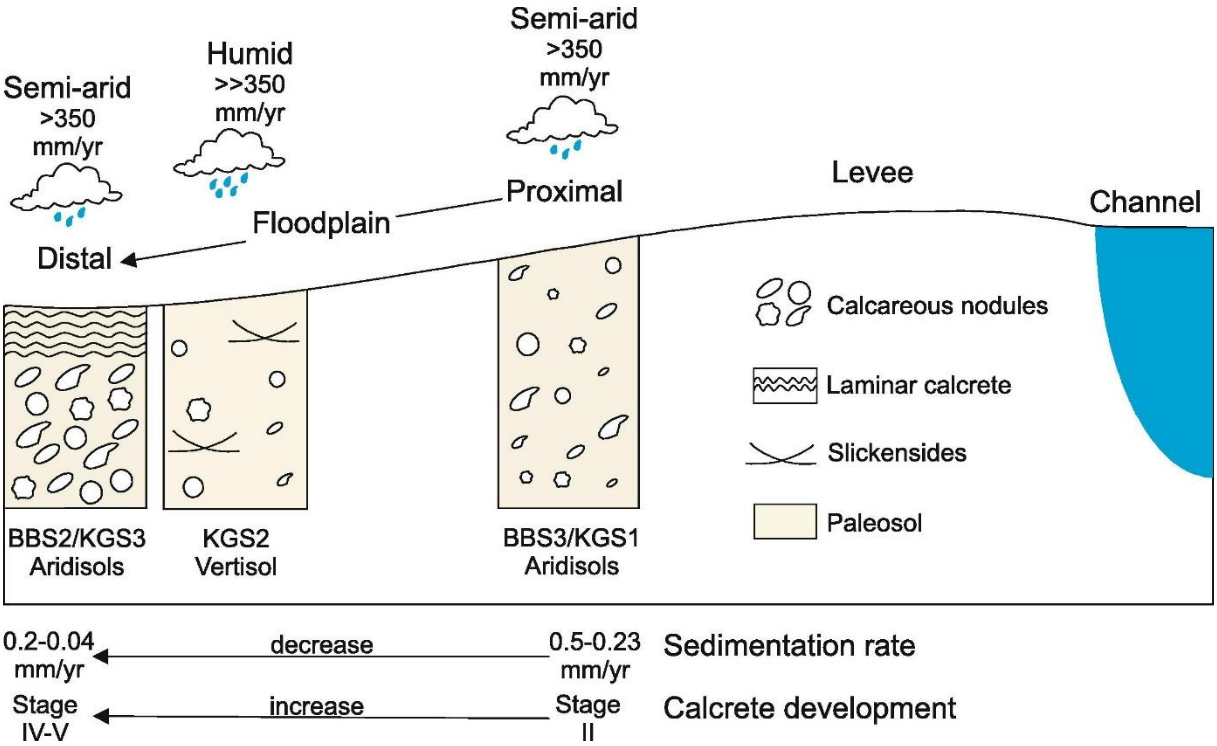
Semi-arid
>350
mm/yr
Humid
>>350
mm/yr
Semi-arid
>350
mm/yr
Proximal
Floodplain
Distal
Levee
Channel
Calcareous nodules
Laminar calcrete
Slickensides
Paleosol
BBS2/KGS3
Aridisols
KGS2
Vertisol
BBS3/KGS1
Aridisols
0.2-0.04
mm/yr
decrease
0.5-0.23
mm/yr
Sedimentation rate
Stage
IV-V
increase
Stage
II
Calcrete development

Figure Caption

Fig. 1: Maps of (A) the middle Atbara River region in eastern Sudan and (B) the geological units of the study area (modified after Mohammednoor et al., 2024).

Fig. 2: Stratigraphic log of the Pleistocene alluvial sediments of Butana Bridge Synthem and Khashm El Girba Synthem near Al Sharafa, with luminescence ages, stratigraphic positions of the studied paleosols (see Fig. 3), pedogenic carbonates and slickensides (modified after Tsukamoto et al., 2022). Abbreviations: cl, clay; si, silt; fs, fine sand; ms, medium sand; cs, coarse sand; gr, granule; pe, pebble; co, cobble; bo, boulder.

Fig. 3: Logs of the Butana Bridge Synthem and Khashm El Girba Synthem paleosols, with pedogenic carbonates, slickensides, stratigraphic positions of pedogenic carbonate (circles filled with black) and oriented paleosol (empty circles) samples, carbonate contents in the matrix, calcrete horizons and their stage of developments in the BBS, KGS1 and KGS3 (modified after Mohammednoor et al., 2024). (A) A 160 cm-thick calcrete horizon in KGS3, consisting of a stage IV-V laminar calcrete overlying a stage II nodular calcrete. (B) Pedogenic carbonates and well-developed slickenside in a 140 cm-thick in the KGS2. (C) A 70 cm-thick, stage II nodular calcrete in KGS1. (D) Stage II nodular calcrete in a 100 cm-thick BBS3. (E) A 110 cm-thick calcrete horizon in BBS2, consisting of a stage IV-V laminar calcrete overlying a stage II nodular calcrete.
Abbreviations: cl, clay; si, silt; vfs, very fine sand; fs, fine sand.

Fig. 4: X-ray diffractograms showing the typical bulk mineralogy of the studied paleosols (sample SU 45 2020; Mohammednoor et al., 2024) and pedogenic carbonates (sample SU 04

2022). Abbreviations: Sm, smectite; Il/Mi, illite/mica; Mo, mordenite; Ho, hornblende; Gy, gypsum; Ch, chlorite; Qtz, quartz; Feld, feldspar; Ca, calcite; Do, dolomite; Ha; halite.

Fig. 5: Micromorphology of pedogenic carbonates. (A) A biotite in a dense micritic matrix, KGS2, plane-polarized light (PPL). (B–C) Desiccation cracks coated and filled with sparitic calcite in a micritic matrix in an Alfa fabric calcrete, KGS1 and KGS3, respectively, cross-polarized light (XPL). (D–E) Quartz (Qtz) and feldspar (Fsp) grains partially surrounded by a pore in a micritic matrix in an Alfa fabric calcrete, BBS3 and BBS2, respectively, XPL. (F) Tissue of decayed root filled with sparitic calcite (petrified root) in a dense micritic matrix in a Beta fabric calcrete, BBS2, PPL. (G) Spherical to ellipsoidal micritic peloids in a dense micritic matrix in a Beta fabric calcrete, BBS2, XPL.

Fig. 6: Micromorphology of paleosols. (A–B) Amphibole and porphyritic basalt grains in a dense siltic matrix, BBS2, PPL and XPL, respectively. (C) Thick calcite void coating, KGS3, XPL. (D) Micritic, mammillate, typic and orthic nodule, KGS3, XPL. (E) Micritic infilling, KGS3, PPL. (F) Calcified root remain influenced by Fe/Mn oxide indicating water saturation or water table fluctuation during a humid period (Vepraskas et al., 2018; Verrecchia and Trombino, 2021), KGS1, XPL. (G) Void clay illuviation, KGS1, XPL. (H) Clay illuviation around quartz (Qtz) grains, KGS2, XPL. (I) Argilliturbation in KGS2, XPL. (J) Angular blocky peds with a high degree of separation, KGS2, XPL. (K) Parallel striated b-fabric caused by shrink-swell processes, indicating a pedogenic slickenside, KGS2, XPL (L) Micritic, typic and disorthic nodule, KGS2, XPL. (M) Septaric nodule, KGS2, XPL.

Fig. 7: Pedogenic carbonate stable carbon and oxygen isotope data. (A) $\delta^{13}C$ and $\delta^{18}O$ values, percentage C_4 plants indicated on the right-side vertical axis. (B) $\delta^{13}C$ values and estimated

fraction of woody cover (f_{wc}) indicated on the right-side vertical axis. (C) $\delta^{18}O$ values of the studied pedogenic carbonate.

Fig. 8: Relationship between the oxygen isotope values of carbonate and water (Zhou and Chafetz, 2010) showing the estimated ranges of $\delta^{18}O$ values of the soil water from which the Butana Bridge Synthem and Khashm El Girba Synthem pedogenic carbonates were formed (a range is not shown for KGS1 because only one sample was measured).

Fig. 9: A comparison between the climatic conditions during the Pleistocene in the study area and paleoclimatic records in the surrounding region in Africa. The red and blue colors of the bars and filled circles symbolize arid and humid climate, respectively. The shaded part in grey scale indicates the agreement of the climate in the middle Atbara River region from ~ 70 ka ago, especially during the LGM, with regional climate records. The paleoclimatic records are based on the Hillaire-Marcel et al. (1986), Abell and Williams (1989), Frédoux (1994), Barker et al. (2007), Cohen et al. (2007), Felton et al. (2007), Lamb et al. (2007), Scholz et al. (2007), Moernaut et al. (2010), Stone et al. (2011), Crosta et al. (2012), Kallweit et al. (2012), Marret et al. (2013), Barrows et al. (2014), Williams et al. (2015), Asrat et al. (2018), Lamb et al. (2018), Cohen and Gibbard (2019), Williams (2019), Leplongeon (2021), Foerster et al. (2022), Gosling et al. (2022) and Mohammednoor et al. (2024). Abbreviations: MIS, Marine Isotope Stage; Med. Sea, Mediterranean Sea; BBS, Butana Bridge Synthem; KGS, Khashm El Girba Synthem; PGP, Penultimate Glacial Period; LGM, Last Glacial Maximum.

Fig. 10: Schematic illustration of the relationship between paleosol profiles and landscape in the vicinity of Al Sharafa. Stage II calcretes in the BBS3 and KGS1 Aridisols formed in proximal floodplains, stage IV-V calcretes in the BBS2 and KGS3 Aridisols, and well-developed vertic horizon in the KGS2 Vertisol formed in distal floodplains.

Table 1: Type of studied samples, sample location, and types of laboratory analyses.

Sample	Type	Location	Methods			
			Carbonate content	X-ray diffraction	Optical microscopy	$\delta^{13}C$ and $\delta^{18}O$
KGS3 Aridisol/Calcisol						
SU 60 2019	Pedogenic carbonate	Al Sharafa	*	*	*	*
SU 76 2022	Orientated paleosol	Al Sharafa			*	
SU 77 2022	Pedogenic carbonate	Al Sharafa	*	*	*	*
KGS2 Vertisol						
SU 61 2019	Pedogenic carbonate	Al Sharafa	*	*	*	*
SU 62 2019	Pedogenic carbonate	Al Sharafa	*	*	*	*
SU 63 2019	Pedogenic carbonate	Al Sharafa	*	*	*	*
SU 01 2022	Pedogenic carbonate	Al Sharafa	*	*	*	*
SU 07 2022	Orientated paleosol	Al Sharafa			*	
SU 08 2022	Orientated paleosol	Al Sharafa			*	
SU 09 2022	Pedogenic crbonate	Al Sharafa	*	*	*	*
SU 10 2022	Orientated paleosol	Al Sharafa			*	
SU 11 2022	Orientated paleosol	Al Sharafa			*	
KGS1 Aridisol/Calcisol						
SU 05 2022	Orientated paleosol	Al Sharafa			*	
SU 27 2022	Pedogenic carbonate	Al Sharafa	*	*	*	*
BBS3 Aridisol/Calcisol						
SU 04 2022	Pedogenic carbonate	Al Sharafa	*	*	*	*
BBS2 Aridisol/Calcisol						
SU 02 2019	Orientated paleosol	Al Sharafa			*	
SU 03 2019	Orientated paleosol	Al Sharafa			*	
SU 05 2020	Pedogenic carbonate	Al Sharafa	*	*	*	*
SU 20 2020	Pedogenic carbonate	Al Sharafa	*	*	*	*
SU 02 2022	Pedogenic carbonate	Al Sharafa	*	*	*	*

SU 03 2022	Pedogenic carbonate	Al Sharafa	*	*	*	*
SU 19 2022	Pedogenic carbonate	Al Sharafa	*	*	*	*
Water						
SU 06 2022	River	Al Sharafa				*
SU 42 2022	River	Al Sharafa				*
SU 43 2022	Groundwater	Al Sharafa				*
SU 51 2022	River	Wadi Turk				*
SU 74 2022	River	Khashm El Girba				*